Renormalizing the quark-meson-diquark model

Hosein Gholami,[1,*] Lennart Kurth,[1,†] Ugo Mire,[2,‡] Michael Buballa,[1,3,§] and Bernd-Jochen Schaefer[2,4,‖]

[1]*Technische Universität Darmstadt, Fachbereich Physik, Institut für Kernphysik, Theoriezentrum, Schlossgartenstrasse 2, D-64289 Darmstadt, Germany*

[2]*Institut für Theoretische Physik, Justus-Liebig-Universität Gießen, 35392 Gießen, Germany*

[3]*Helmholtz Forschungsakademie Hessen für FAIR (HFHF), GSI Helmholtzzentrum für Schwerionenforschung, Campus Darmstadt, D-64289 Darmstadt, Germany*

[4]*Helmholtz Forschungsakademie Hessen für FAIR (HFHF), GSI Helmholtzzentrum für Schwerionenforschung, Campus Gießen, 35392 Gießen, Germany*

(Received 28 July 2025; accepted 6 May 2026; published 11 June 2026)

We present a comprehensive study of the two-flavor quark-meson-diquark (QMD) model by comparing a renormalization approach with a renormalization-group (RG) consistent mean-field formulation based on the functional renormalization group (FRG). The renormalized QMD model allows analytical investigations of key quantities such as the zero-temperature diquark gap and the critical temperature for color superconductivity, ultimately reproducing the exact BCS relation in the high-density limit. We carry out the same analysis for different schemes of RG-consistent QMD models. We show that the RG-consistent approach yields a phase diagram and thermodynamic properties qualitatively similar to those of the renormalized model, provided both are embedded within a unified scheme that ensures consistent vacuum properties. In particular, both treatments recover the Stefan-Boltzmann limit at high densities. On the other hand, whether the BCS relation for the critical temperature is satisfied depends on the details of the RG-consistent setup. Our results highlight the relevance of renormalization and RG-consistent methods for accurately capturing the thermodynamics of QMD and related effective models with diquark degrees of freedom.

DOI: 10.1103/bx12-6tt6

I. INTRODUCTION

Quantum chromodynamics (QCD) is the fundamental theory of the strong interaction among quarks and gluons. In the low-energy regime, however, QCD becomes inherently nonperturbative, making direct analytical calculations extremely challenging. Over the years, a variety of nonperturbative tools have been developed to study QCD in this regime. Notably, lattice QCD simulations [1] and continuum functional methods (such as Dyson-Schwinger equations [2] and the functional renormalization group [3]) have provided important insights into the QCD phase structure. Despite these advances, first-principles calculations remain challenging, particularly for the thermodynamics of QCD at finite density, motivating the use of effective models to capture its essential low-energy physics.

Effective models of QCD are designed to respect its symmetries and replicate the dynamics of the full theory, enabling the study of phenomena such as spontaneous chiral symmetry breaking and hadronization within a more manageable framework. Two prominent examples are the Nambu–Jona-Lasinio (NJL) and the quark-meson model, also known as the linear sigma model coupled to quarks. These models dynamically generate constituent quark masses through chiral condensates and successfully capture many qualitative features of low-energy QCD. They have been widely employed to investigate the QCD phase diagram and its transition properties [4–6].

At high baryon density color-superconducting (CSC) phases are expected to emerge, i.e., phases where quarks are paired in so-called diquark condensates [7]. Most prominent examples are the two-flavor superconducting (2SC) phase, where the pairs consists of up and down quarks, and the color-flavor locked (CFL) phase, where also strange quarks are involved. While the quark-meson model and earlier versions of the NJL model account for quark-antiquark condensates only, CSC phases can straightforwardly be described within the NJL model by adding the appropriate quark-quark interactions [4,8,9].

*Contact author: mohammadhossein.gholami@tu-darmstadt.de
†Contact author: lennart.kurth@stud.tu-darmstadt.de
‡Contact author: ugo.louis.tryphon.mire@physik.uni-giessen.de
§Contact author: michael.buballa@tu-darmstadt.de
‖Contact author: bernd-jochen.schaefer@uni-giessen.de

Similarly, a natural extension of the quark-meson model to enable the modeling of CSC is the inclusion of diquark degrees of freedom. This leads to the so-called quark-meson-diquark (QMD) model [10–12], first introduced in the context of two-color QCD [13–15], whose effective Lagrangian incorporates not only mesonic fields (such as the sigma (σ) and pions ($\vec{\pi}$), associated with the chiral symmetry) but also explicit complex-valued diquark fields (Δ, Δ^*) representing correlated quark–quark and antiquark-antiquark pairs. The diquark fields can condense in the color-antitriplet channel, providing a description of the color-superconducting phase of quark matter [7].

Despite their successes, NJL-type models are nonrenormalizable. As a result, a momentum cutoff (or another regularization scheme) must be introduced to handle ultraviolet (UV) divergences, and physical predictions can, in general, depend on the choice of the regularization scheme. In particular, a naïve cutoff regularization can induce significant artifacts, making certain observables unphysically sensitive to the regulator [16].

The quark–meson model, which can be regarded as a bosonized NJL model with Yukawa couplings, is renormalizable. However, when treated with a simple cutoff and without proper renormalization, it may exhibit spurious regulator dependencies. Over the years, various techniques have been developed to mitigate these issues and ensure proper renormalization-group (RG) behavior in effective models.

One strategy to eliminate cutoff artifacts is renormalization—explicitly incorporating a dependence of the bare model parameters (such as couplings and masses) on the regulator scale so that all divergent contributions are absorbed into redefinitions of these parameters. In practice, this involves the introduction of counterterms to ensure that physical observables remain finite and independent of the UV cutoff eventually. As a (perturbatively) renormalizable theory, the QMD model permits a fully renormalized formulation in which all UV divergences are absorbed into the bare parameters of the Lagrangian (at least on the mean-field level, where bosonic fluctuations are neglected). This issue was recently discussed in Ref. [17] and explicitly demonstrated using dimensional regularization in Ref. [11]—a scheme often favored for preserving symmetries, particularly Lorentz invariance. At finite temperature and chemical potential, however, Lorentz symmetry is explicitly broken, reducing the advantages of this scheme. In the present work, we instead employ a technically simpler three-momentum cutoff, which eventually yields more tractable expressions.

An alternative and powerful approach is provided by the functional renormalization group (FRG) formalism, pioneered by Wetterich [18], which allows for an RG-consistent formulation of the model. In this FRG-based treatment, a scale-dependent effective action is introduced, with the requirement that physical quantities in the infrared (IR) of the flow remain independent of the chosen regulator cutoff. Such FRG-improved schemes have been applied to low-energy QCD models, see e.g. [10,17,19]. Because of its generality, the RG-consistent treatment has two key advantages: it extends to nonrenormalizable models, and its implementation is usually simpler as it does not require renormalization conditions.

The QMD model can be analyzed using an RG-consistent mean-field methodology, ensuring that cutoff artifacts are canceled out by flow corrections. In Ref. [17] this method was applied to the three-flavor NJL model, and it was found that the RG consistent treatment does not only remove obvious cutoff artifacts, like decreasing diquark condensates with increasing chemical potentials, but also less expected ones concerning the ordering of the color-superconducting phases [20]. It should be noted, however, that the NJL model is nonrenormalizable and, as a consequence, the cutoff cannot be chosen freely but is the result of the parameter fit in vacuum, e.g., Ref. [21]. The RG consistent treatment applied in Ref. [17] then removes cutoff artifacts related to medium scales (temperatures or chemical potentials) of the order of the cutoff. However, the RG-consistent treatment requires special care with the divergences that arise at finite chemical potential, often referred to as medium-induced divergences. Related to this, there is some scheme dependence in the NJL model due to the treatment of the medium-induced divergences. Different subtraction schemes lead to variations in the results, including changes in the predicted phase diagram.

As a consequence of these scheme ambiguities, it is thus of great interest to better understand the RG-consistent treatment, and the QMD model provides a controlled setup for such an analysis. In the mean-field approximation (MFA) of the QMD model, the initial UV scale can be chosen arbitrarily large.[1] For sufficiently large values the results of the "RG consistent treatment" then become fully RG invariant, i.e., independent of the initially chosen UV scale and identical to the results of the fully renormalized model.[2] In this paper, however, we deliberately choose a relatively small value of the initial UV scale, similar to a typical NJL cutoff, and then compare the results obtained with different schemes of the RG consistent treatment with the "exact" ones of the renormalized formulation. In this way, the QMD model serves as a controlled testing ground

[1]At the one-loop level, the renormalized vacuum quark contribution renders the effective potential unbounded from below for sufficiently large values of the order parameter. This instability is a truncation artifact, which can be resolved by the inclusion of higher-order loop contributions, see, e.g., Refs. [22,23], and is not relevant for the present analysis.

[2]We emphasize that this only holds true in the mean-field approximation. In the presence of meson and diquark fluctuations, RG-consistency simply ensures UV-cutoff independence up to the Landau pole whose cutoff location defines the UV-consistency scale of the QMD model. See also Ref. [10] for more details.

for directly contrasting these schemes, thereby giving a hint on their quality also for other models.

For a meaningful comparison, we fix the model parameters in both approaches to the same physical vacuum observables, such as the pion mass, decay constant, and vanishing diquark gap in vacuum. We then analyze how the predictions of these two treatments diverge away from the vacuum and in particular at finite chemical potential and temperature.

An important advantage of implementing an explicit renormalization procedure (or an RG-consistent approximation) is that it enables us to derive analytical results, providing benchmarks for the model's predictions under extreme conditions. In particular, we demonstrate that in the high-density limit, both approaches recover the expected BCS relation between the zero-temperature diquark gap, $\Delta_{\mathrm{gap}}(T=0)$, and the critical temperature, T_c, of the superconducting phase. Furthermore, we verify that as the quark chemical potential μ increases, both treatments approach the free-quark Stefan-Boltzmann limit for thermodynamic quantities, ensuring consistency with standard thermodynamic expectations. On the other hand, we find that, in the QMD model, the diquark gap asymptotically approaches a constant at large μ, whereas in full QCD, the pairing gap is expected to diverge in the limit $\mu \to \infty$ despite the weakening of the attractive interaction at high density [24,25]. Nonetheless, the ability to obtain analytic high-density results within the QMD framework remains valuable, as it allows us to pinpoint the limitations of the model and identify the missing physics necessary for a more accurate description of dense quark-matter.

Our approach is based on the MFA. However we note that, several alternative methods are being developed to access the intermediate-density regime beyond the MFA. In particular, these include approaches based on Dyson-Schwinger equations [26–31], the FRG [15,32,33] and holographic QCD [34].

The remainder of this paper is organized as follows. In Sec. II we introduce the QMD model and its field content, describing the quark, meson, and diquark sectors and introduce the standard regularized mean-field approximation. In Sec. III, we present the renormalization scheme for the QMD model, demonstrating how divergent vacuum contributions can be absorbed into the couplings and discuss the determination of the model parameters from vacuum observables. Sec. IV is devoted to the FRG approach and the implementation of the RG-consistent mean-field approximation, with special attention to the treatment of medium-dependent divergences at finite chemical potential. In Sec. V we present analytical results for the different approximations of QMD model considered in this work. In particular, we derive analytically the asymptotic behavior of the diquark condensate and the BCS relation. In Sec. VI we compare numerical results for the renormalized and RG-consistent approaches, examining the resulting phase diagram and thermodynamic properties such as the diquark gap, critical temperatures, and pressure. Finally, we summarize our findings in Sec. VII, highlighting the agreements and differences between the two treatments and offering some outlook for future investigations.

II. QUARK-MESON-DIQUARK MODEL

In this section, we introduce the $N_f = 2$ quark-meson-diquark model, which serves as the foundation of our analysis. This model describes the interaction between the quark fields q and $\bar{q}$ and the effective degrees of freedom associated with the σ and $\vec{\pi}$ mesons, as well as the diquark fields Δ and Δ^*. In this work we consider $N_c = 3$ colors and $N_f = 2$ flavors. Accordingly, the condensation of the diquark fields corresponds to a 2SC phase.

The action of the model in the Euclidean space at finite temperature $\beta = 1/T$ is given by

$$S[\bar{q},q,\phi,\Delta,\Delta^*] = \int_0^\beta dx_4 \int d^3x \Big\{ \bar{q}[Z_q(\partial\!\!\!/ - \mu\gamma_4) + g_\phi(\sigma + i\gamma_5\vec{\pi}\cdot\vec{\tau})]q + \frac{1}{2} g_\Delta(\Delta_a \bar{q}\gamma_5\tau_2 i\epsilon_a C\bar{q}^{\mathsf{T}} - \Delta_a^* q^{\mathsf{T}} C\gamma_5\tau_2 i\epsilon_a q) + \frac{Z_\phi}{2}(\partial_\mu\phi)(\partial_\mu\phi) + Z_\Delta(\partial_\mu + 2\mu\delta_{\mu 4})\Delta_a^*(\partial_\mu - 2\mu\delta_{\mu 4})\Delta_a + U(\phi^2,|\Delta|^2) - c\sigma \Big\}. \tag{1}$$

Here, the quark fields q and $\bar{q}$ are understood as vectors in color, flavor and Dirac space. The mesonic fields are grouped into the $O(4)$-symmetric chiral field $\phi^{\mathsf{T}} = (\sigma, \vec{\pi}^{\mathsf{T}})$ which provides a convenient basis for constructing the chirally invariant quantity $\phi^2 = \sigma^2 + \vec{\pi}^2$. The complex-valued diquark fields Δ and Δ^* are understood as vectors in color space and their components Δ_a and Δ_a^* carry a color index $a = 1, 2, 3$.

Throughout this work, we generally omit field indices for readability, except for the diquark fields, where the color indices are always shown explicitly. Additionally, we define the diquark invariant as $|\Delta|^2 = |\Delta_1|^2 + |\Delta_2|^2 + |\Delta_3|^2$. The Euclidean γ-matrices are defined such that $\{\gamma_\mu, \gamma_\nu\} = 2\delta_{\mu\nu}$ and the charge conjugation matrix reads $C = \gamma_2\gamma_4$. We also introduced the fully antisymmetric tensor in color space $(\epsilon_a)_{bc} = \epsilon_{abc}$ and the three Pauli matrices τ_i acting in flavor space.

In Eq. (1), the kinetic terms of the quark, meson and diquark field are included with their associated wave-function renormalizations Z_q, Z_ϕ and Z_Δ. In particular, note the structure of the diquark kinetic term, which explicitly couples to the chemical potential μ because the diquark field carries a nonzero $U(1)_B$ charge.

We collect all bosonic interaction terms in a potential $U(\phi^2, |\Delta|^2)$, which depends only on the chiral invariant ϕ^2 and the diquark invariant $|\Delta|^2$. The most general form of this potential, which includes all relevant and marginal couplings, is given by

$$U(\phi^2, |\Delta|^2) = \frac{1}{2} m_\phi^2 \phi^2 + \frac{1}{4}\lambda_\phi \phi^4 + m_\Delta^2 |\Delta|^2 + \lambda_\Delta |\Delta|^4 + \frac{1}{2}\lambda_{\mathrm{mix}} \phi^2 |\Delta|^2. \quad (2)$$

In practical applications, it is common to omit some of the couplings due to the lack of physical observables sensitive to diquark pairing, which limits constraints on these couplings. A typical and simple approximation sets $\lambda_\Delta = \lambda_{\mathrm{mix}} = 0$. However, as we will show in Sec. III, all of these couplings are essential for renormalization. We revisit the issue of missing constraints in Sec. VI A.

A. Regularized mean-field approximation

A common approach for studying the model's thermodynamic properties is the mean-field approximation, where the bosonic fields are assumed to take constant field configurations: $\phi^\mathsf{T} = (\sigma, \vec{0}^\mathsf{T})$ and $\Delta_a = \Delta\delta_{a3}$ with $\sigma \in \mathbb{R}$ and $\Delta \in \mathbb{R}$. Note that in a slight abuse of notation we use the same symbol for the homogeneous field configuration and for the space-time dependent field. A nonvanishing value of Δ singles out a direction in color space and thus breaks the global SU(3) color symmetry of the action Eq. (1) down to SU(2). Correspondingly, since Δ_3 couples to the quarks via ϵ_3, only the quarks of the first two colors (usually called "red" and "green") are affected by the condensation, while the third color ("blue") is not.

Then, neglecting all bosonic fluctuations in the path integral, the effective thermodynamic potential of the model can be computed as

$$\Omega^{\mathrm{eff}}_{\mathrm{reg}}(\sigma, \Delta; T, \mu) = U(\sigma^2, \Delta^2) - c\sigma - 4Z_\Delta \mu^2 \Delta^2 + L_\Lambda(m_q, \Delta_{\mathrm{gap}}; T, \mu), \quad (3)$$

where

$$L_\Lambda(m_q, \Delta_{\mathrm{gap}}; T, \mu) = -2N_f \int_{|\vec{p}|<\Lambda} \{E_q^+ + E_q^- + \epsilon_q + 2T\ln(1 + e^{-E_q^+/T}) + 2T\ln(1 + e^{-E_q^-/T}) + T\ln(1 + e^{-\epsilon_q^+/T}) + T\ln(1 + e^{-\epsilon_q^-/T})\}, \quad (4)$$

stands for the quark loop contribution with the dispersion relations

$$E_q^\pm = \sqrt{\epsilon_q^{\pm 2} + \Delta_{\mathrm{gap}}^2}, \quad (5)$$

and

$$\epsilon_q^\pm = \epsilon_q \pm \mu \quad \text{with} \quad \epsilon_q = \sqrt{\vec{p}^2 + m_q^2}. \quad (6)$$

The quark mass m_q and the Fermi-surface gap Δ_{gap} are related to the homogeneous field configurations through

$$m_q = g_\phi \sigma \quad \text{and} \quad \Delta_{\mathrm{gap}} = g_\Delta \Delta, \quad (7)$$

and correspond to the physical implications of the chiral and diquark condensate on the quark sector. In particular, the dependence of L_Λ on m_q and Δ_{gap}, and not σ or Δ individually, highlights that it originates from the quark physics.

In general, we use a short-hand notation for momentum integrals, where the integral index specifies any possible cutoffs

$$\int_{\vec{p}} \equiv \int \frac{d^3p}{(2\pi)^3}, \quad \text{and} \quad \int_{|\vec{p}|<\Lambda} \equiv \int \frac{d^3p}{(2\pi)^3}\theta(\Lambda^2 - \vec{p}^2). \quad (8)$$

Thus, the effective potential Eq. (3) consists of the tree-level bosonic potential with the explicit symmetry breaking term, a quadratic diquark contribution from the diquark kinetic term that still depends on the chemical potential, and a quark loop contribution. The divergent quark loop is regularized with a three-momentum cutoff, $|\vec{p}| < \Lambda$.[3] We refer to Eq. (3) as the *regularized* mean-field approximation (regMFA) and use the subscript reg accordingly.

Note that in obtaining Eq. (3) we implicitly chose to set $Z_q = 1$. At the mean-field level, the quark wave function renormalization does not receive any loop contribution and only contributes through a rescaling of the Yukawa couplings g_ϕ and g_Δ. As such any dependency on Z_q can be safely removed by a rescaling of g_ϕ and g_Δ, which is fully equivalent to choosing $Z_q = 1$ in Eq. (1). This is in contrast to the meson and diquark wave function renormalizations which receive a loop contribution. As we only consider homogeneous condensates, the meson wave function Z_ϕ does not contribute to the effective potential and can safely be ignored. However, the diquark wave

[3]In nonsuperconducting models, it is common to only regularize the divergent vacuum contribution, leading to reduced cutoff artifacts. However, for superconducting models the dispersion relation $E_q^\pm$ depends on the chemical potential and a separation into a divergent vacuum contribution and a convergent medium contribution is not possible. For details, see Ref. [17].

function renormalization Z_Δ contributes to the effective potential and must, without further approximations, be considered.

The three-momentum cutoff regularization scheme is often used in the literature due to its simplicity and the fact that at finite T and μ the Lorentz symmetry is already explicitly broken. Only the $T = 0$ contribution of the quark loop diverges, as can be seen from the asymptotic expansion

$$\begin{aligned} &L_\Lambda(m_q, \Delta_{\mathrm{gap}}; T, \mu) \\ &\underset{\Lambda\to\infty}{\simeq} -\frac{3}{2\pi^2}\Lambda^4 - \frac{(3m_q^2 + 2\Delta_{\mathrm{gap}}^2)}{2\pi^2}\Lambda^2 \\ &\quad + \left(\frac{3m_q^4}{4\pi^2} + \frac{m_q^2\Delta_{\mathrm{gap}}^2}{\pi^2} + \frac{\Delta_{\mathrm{gap}}^4}{2\pi^2} - \mu^2\frac{2\Delta_{\mathrm{gap}}^2}{\pi^2}\right)\ln\Lambda. \end{aligned} \tag{9}$$

Note in particular the presence of a μ^2 divergence, which we call a *medium divergence*.

The regularized effective potential Eq. (3) suffers from cutoff artifacts due to the absence of high-momentum modes $|\vec{p}| > \Lambda$. A straightforward yet naïve solution is to choose Λ much larger than any physical scale in the system. However, this procedure presents two difficulties.

The first difficulty is technical: the vacuum and medium contributions to the effective potential diverge as $\Lambda \to \infty$ [see Eq. (9)]. Due to these divergences, fixing the bare parameters as $\Lambda \to \infty$ becomes a fine-tuning problem. The renormalization of the model is the procedure that resolves this fine-tuning issue.

The second difficulty is conceptual: in nonrenormalizable models like the NJL model, the cutoff Λ is an intrinsic parameter—similar to the bare couplings—and is chosen to reproduce vacuum phenomenology. As a result, it may be impossible to eliminate all cutoff artifacts by simply tuning Λ. RG-consistency offers a way to address this issue, enabling the removal of cutoff artifacts in both renormalizable and nonrenormalizable models [10,17]. We are thus faced with two approaches that aim to achieve the same goal. It is therefore natural to compare them directly.

In the following Sec. III, we present a straightforward renormalization procedure to eliminate the cutoff dependence. Then, Sec. IV briefly reviews the RG-consistency approach introduced in Ref. [10] and discusses how it handles medium divergences. Finally, in Secs. V and VI, we compare the predictions of the two methods using both analytical and numerical results.

III. RENORMALIZED APPROACH

In the renormalized approach, the bare parameters are assumed to depend on the cutoff scale Λ such that the effective potential remains finite as $\Lambda \to \infty$. To detail this, we derive in Sec. III A the asymptotic behavior of the couplings required for finiteness of the potential. In Sec. III B, we present an explicit strategy for implementing the renormalized mean-field approximation.

A. Asymptotic expansion

We begin by noting that all divergent contributions to the effective potential take the form shown in Eq. (9). By rewriting this expression in terms of the condensates and comparing it to the various bare couplings in $U(\phi^2, |\Delta|^2)$, we find that all purely bosonic bare couplings are required to absorb the divergences—except for the medium divergence, which can be handled via the wave function renormalization of the diquarks.

Promoting all couplings and the diquark wave function renormalization in the regularized potential $\Omega_{\mathrm{reg}}^{\mathrm{eff}}$, Eq. (3), to functions of the cutoff Λ, the renormalized effective potential $\Omega_{\mathrm{ren}}^{\mathrm{eff}}$ is eventually obtained by taking the limit $\Lambda \to \infty$. An asymptotic expansion of the renormalized potential together with Eq. (9) then yields

$$\begin{aligned} &\Omega_{\mathrm{ren}}^{\mathrm{eff}}(\sigma, \Delta; T, \mu) \\ &\underset{\Lambda\to\infty}{\simeq} \frac{1}{2}\left[\lambda_{\mathrm{mix}}(\Lambda) + \frac{2g_\phi^2 g_\Delta^2}{\pi^2}\ln\Lambda\right]\sigma^2\Delta^2 \\ &\quad + \frac{1}{2}\left[m_\phi^2(\Lambda) - \frac{3g_\phi^2}{\pi^2}\Lambda^2\right]\sigma^2 + \frac{1}{4}\left[\lambda_\phi(\Lambda) + \frac{3g_\phi^4}{\pi^2}\ln\Lambda\right]\sigma^4 \\ &\quad + \left[m_\Delta^2(\Lambda) - \frac{g_\Delta^2}{\pi^2}\Lambda^2\right]\Delta^2 + \left[\lambda_\Delta(\Lambda) + \frac{g_\Delta^4}{2\pi^2}\ln\Lambda\right]\Delta^4 \\ &\quad - 4\left[Z_\Delta(\Lambda) + \frac{g_\Delta^2}{2\pi^2}\ln\Lambda\right]\mu^2\Delta^2 - \frac{3}{2\pi^2}\Lambda^4. \end{aligned} \tag{10}$$

From Eq. (10), we conclude that maintaining a finite effective potential as $\Lambda \to \infty$ requires the bare couplings to scale with Λ as follows:

$$m_\phi^2(\Lambda) = \frac{3g_\phi^2}{\pi^2}\Lambda^2 + \mathcal{O}(1), \tag{11}$$

$$m_\Delta^2(\Lambda) = \frac{g_\Delta^2}{\pi^2}\Lambda^2 + \mathcal{O}(1), \tag{12}$$

$$Z_\Delta(\Lambda) = -\frac{g_\Delta^2}{2\pi^2}\ln\Lambda + \mathcal{O}(1), \tag{13}$$

$$\lambda_\phi(\Lambda) = -\frac{3g_\phi^4}{\pi^2}\ln\Lambda + \mathcal{O}(1), \tag{14}$$

$$\lambda_{\mathrm{mix}}(\Lambda) = -\frac{2g_\phi^2 g_\Delta^2}{\pi^2}\ln\Lambda + \mathcal{O}(1), \tag{15}$$

$$\lambda_\Delta(\Lambda) = -\frac{g_\Delta^4}{2\pi^2}\ln\Lambda + \mathcal{O}(1). \tag{16}$$

The remaining parameters g_ϕ, g_Δ, and c stay finite, as they do not receive loop corrections at mean-field level, and can therefore be treated as cutoff-independent.

B. Vacuum matching procedure

We now outline a concrete strategy to fix the model parameters. In general, determining all couplings and their cutoff dependence requires a sufficient number of constraints, typically obtained by fitting a suitable set of vacuum parameters. If the analysis is restricted to the homogeneous phase diagram and momentum-dependent observables (such as the pole masses) are not of interest, the mesonic wave function renormalization Z_ϕ does not enter the calculation. In contrast, the diquark wave function renormalization Z_Δ must be taken into account, as it appears explicitly in the effective potential through its coupling to the chemical potential, as previously noted.

The importance of wave function renormalization for the renormalizability of such effective models at finite density was recently emphasized in Refs. [17,35]. Particularly in Ref. [35] and in the context of the two-flavor quark-meson model at finite isospin density, it was shown within an RG-invariant mean-field approximation that, once a single RG-invariant scale is matched to lattice data, the resulting equation of state and phase diagram agree quantitatively with modern lattice simulations over a broad range of μ_I.

As already mentioned, g_ϕ, g_Δ and c receive no loop contributions in MFA. They can therefore be fixed directly, without requiring corresponding vacuum parameters. This leaves six couplings from Eqs. (11) to (16) that must be determined. To illustrate the procedure, we fix them using a set of *vacuum parameters*—a process we refer to as the *vacuum matching procedure*. The chosen set of parameters is

$$\mathcal{P}_{\mathrm{vac}} = \{\tilde{f}_\pi, \tilde{m}_\sigma^2, \tilde{m}_\Delta^2, \tilde{Z}_\Delta, \tilde{\lambda}_{\mathrm{mix}}, \tilde{\lambda}_\Delta\}. \tag{17}$$

In Table I, we list the vacuum parameters, their definitions in terms of the effective action, and their physical interpretations. It is worth noting that this choice of parameters is not unique—alternative sets of vacuum parameters could be used. In particular, no parameter is directly associated with λ_ϕ, which will instead be fixed through a combination of $\tilde{f}_\pi$ and $\tilde{m}_\sigma^2$, as discussed in Appendix A.

TABLE I. Vacuum parameters and their definitions in terms of the effective action, along with their physical interpretation (in vacuum). The subscript "vac" denotes evaluation at $\sigma = \tilde{f}_\pi$ and $\Delta = 0$ in vacuum.

Vacuum parameters	Physical interpretation
$\tilde{f}_\pi = \langle\sigma\rangle_{\mathrm{vac}}$	Pion decay constant
$\tilde{m}_\sigma^2 = (\partial_\sigma^2 \Omega^{\mathrm{eff}})\vert_{\mathrm{vac}}$	Sigma mass
$\tilde{m}_\Delta^2 = \frac{1}{2}(\partial_\Delta^2 \Omega^{\mathrm{eff}})\vert_{\mathrm{vac}}$	Diquark mass
$\tilde{\lambda}_{\mathrm{mix}} = \frac{1}{2}(\partial_\sigma^2 \partial_\Delta^2 \Omega^{\mathrm{eff}})\vert_{\mathrm{vac}}$	Δ–σ scattering amplitude
$\tilde{\lambda}_\Delta = \frac{1}{24}(\partial_\Delta^4 \Omega^{\mathrm{eff}})\vert_{\mathrm{vac}}$	Δ–Δ scattering amplitude
$\tilde{Z}_\Delta = -\frac{1}{16}(\partial_\mu^2 \partial_\Delta^2 \Omega^{\mathrm{eff}})\vert_{\mathrm{vac}}$	Diquark wave function renormalization

Note that the diquark wave function renormalization, Z_Δ, is associated with single particle states and, in this regard, is not directly linked to any physical observable. One can always fix Z_Δ to an arbitrary constant at a fixed scale, which in turn rescales the fields and consequently modifies the values of other model couplings. Here, we choose to fix this parameter in vacuum. In contrast, the remaining parameters can be related to physical observables involving multiparticle states that are, for example, realized through certain scattering or decay processes. To this end, we define a set of vacuum parameters that can be associated with these physical quantities.

The pion decay constant is directly related to the chiral condensate in vacuum[4]

$$\tilde{f}_\pi = \langle\sigma\rangle_{\mathrm{vac}}, \tag{18}$$

which is determined as the solution of the gap equation evaluated for vanishing diquark condensate

$$\frac{\partial \Omega_{\mathrm{ren}}^{\mathrm{eff}}(\sigma, \Delta = 0; T = 0, \mu = 0)}{\partial \sigma} = 0. \tag{19}$$

For $\Delta = 0$ we can use Eq. (3) and obtain

$$m_\phi^2 \tilde{f}_\pi + \lambda_\phi \tilde{f}_\pi^3 + \frac{\partial L_\Lambda(m_q, \Delta_{\mathrm{gap}} = 0; T = 0, \mu = 0)}{\partial \sigma} - c = 0. \tag{20}$$

With the definitions of the remaining vacuum parameters, one can derive a linear system of equations that allows one to express the bare parameters in terms of vacuum quantities. Substituting these expressions into the effective potential and subsequently taking the limit $\Lambda \to \infty$ yields a renormalized form of the effective potential. The details of this procedure are presented in Appendix A. The renormalized potential takes the following form

$$\begin{aligned}\Omega_{\mathrm{ren}}^{\mathrm{eff}}(\sigma, \Delta; T, \mu) = {} & U_{\mathrm{ren}}(\sigma^2, \Delta^2) - c\sigma - 4\tilde{Z}_\Delta \Delta^2 \mu^2 \\ & + L_{\mathrm{ren}}(m_q, \Delta_{\mathrm{gap}}; T, \mu),\end{aligned} \tag{21}$$

where U_{ren} is the renormalized potential contribution, now expressed in terms of the vacuum parameters as

[4]This identity assumes that the residue of the pion propagator at its pole is normalized to one. This condition can always be achieved by choosing an appropriate $\tilde{Z}_\phi$, which we have implicitly done here. In contrast, in Refs. [36,37], the choice $Z_\phi = 1$ was made. The relation between the pion decay constant and the chiral condensate was then given by $f_\pi = \sigma/\sqrt{Z_\pi}$, where Z_π^2 is the residue of the dressed pion propagator at the pion pole.

$$U_{\mathrm{ren}}(\sigma^2,\Delta^2)=\tilde{\lambda}_\Delta\Delta^4+\left(-\frac{\tilde{m}_\sigma^2}{4}+\frac{3c}{4\tilde{f}_\pi}\right)\sigma^2+\left(-\frac{c}{8\tilde{f}_\pi^3}+\frac{\tilde{m}_\sigma^2}{8\tilde{f}_\pi^2}\right)\sigma^4+\frac{1}{2}\tilde{\lambda}_{\mathrm{mix}}\sigma^2\Delta^2+\left(\tilde{m}_\Delta^2-\frac{1}{2}\tilde{\lambda}_{\mathrm{mix}}\tilde{f}_\pi^2\right)\Delta^2, \tag{22}$$

and $L_{\mathrm{ren}}(m_q,\Delta_{\mathrm{gap}};T,\mu)$ represents the renormalized loop contribution

$$\begin{aligned}L_{\mathrm{ren}}(m_q,\Delta_{\mathrm{gap}};T,\mu)=2N_f\int_{\vec{p}}\Bigg\{&3p+\frac{\Delta_{\mathrm{gap}}^2\mu^2}{\epsilon_{q,\mathrm{vac}}^3}-\frac{\Delta_{\mathrm{gap}}^4}{4\epsilon_{q,\mathrm{vac}}^3}+\frac{\Delta_{\mathrm{gap}}^2}{2\epsilon_{q,\mathrm{vac}}^5}p^2(2p^2+5m_{q,\mathrm{vac}}^2)-\frac{\Delta_{\mathrm{gap}}^2m_q^2}{2\epsilon_{q,\mathrm{vac}}^5}(p^2-2m_{q,\mathrm{vac}}^2)\\&+\frac{3m_q^2}{4\epsilon_{q,\mathrm{vac}}^3}(2p^2+3m_{q,\mathrm{vac}}^2)-\frac{3m_q^4}{8\epsilon_{q,\mathrm{vac}}^3}-E_q^+-E_q^-+\epsilon_q\\&-2T\ln\left(1+e^{-E_q^+/T}\right)-2T\ln\left(1+e^{-E_q^-/T}\right)-T\ln\left(1+e^{-\epsilon_q^+/T}\right)-T\ln\left(1+e^{-\epsilon_q^-/T}\right)\Bigg\},\end{aligned} \tag{23}$$

where we introduced

$$m_{q,\mathrm{vac}}=g_\phi\tilde{f}_\pi\quad\text{and}\quad\epsilon_{q,\mathrm{vac}}=\sqrt{p^2+m_{q,\mathrm{vac}}^2}. \tag{24}$$

It includes both the standard loop contribution and the additional counterterm contribution arising from the bare parameters. This results in a finite expression for the effective potential in the limit $\Lambda\to\infty$.

Using this, we can define the gap equations

$$\left.\frac{\partial\Omega_{\mathrm{ren}}^{\mathrm{eff}}(\sigma,\Delta;T,\mu)}{\partial\sigma}\right|_{\bar{\sigma},\bar{\Delta}}=0, \tag{25a}$$

$$\left.\frac{\partial\Omega_{\mathrm{ren}}^{\mathrm{eff}}(\sigma,\Delta;T,\mu)}{\partial\Delta}\right|_{\bar{\sigma},\bar{\Delta}}=0. \tag{25b}$$

By solving these two equations simultaneously, we get the physical gap solutions $\bar{\sigma}(T,\mu)$, and $\bar{\Delta}(T,\mu)$, also denoted as the condensates in the following and the thermodynamic potential is then obtained by inserting these solutions back into the effective potential. What is now missing are the values of the vacuum parameters we have introduced. We will come back to them in Sec. VI A.

Lastly, we note that one could, if desired, absorb the wave function renormalization factor $\tilde{Z}_\Delta$ via the field redefinition $\Delta\to\Delta\tilde{Z}_\Delta^{-1/2}$. One can simultaneously rescale the diquark Yukawa coupling as $g_\Delta\to g_\Delta\tilde{Z}_\Delta^{1/2}$, the diquark vacuum curvature mass as $\tilde{m}_\Delta^2\to\tilde{m}_\Delta^2\tilde{Z}_\Delta$, the meson-diquark vacuum scattering coupling as $\tilde{\lambda}_{\mathrm{mix}}\to\tilde{\lambda}_{\mathrm{mix}}\tilde{Z}_\Delta$ and the diquark vacuum scattering coupling as $\tilde{\lambda}_\Delta\to\tilde{\lambda}_\Delta\tilde{Z}_\Delta^2$. In that representation the RG-invariant combinations $\Delta_{\mathrm{gap}}=g_\Delta\Delta$, $\tilde{m}_\Delta^2\Delta^2$, $\tilde{\lambda}_{\mathrm{mix}}\Delta^2\phi^2$ and $\tilde{\lambda}_\Delta\Delta^4$ remain unchanged. Proceeding similarly for the mesons, one can write the effective action EQ. (21) in an RG invariant way. However, in this work and for clarity we keep the original normalization, with $\tilde{Z}_\Delta$ explicit. Conversely, ignoring the $\tilde{Z}_\Delta$ factor when quoting the vacuum parameters, e.g. the vacuum curvature masses in Table I, would misidentify the intended parameter set. Since this work enforces a common vacuum baseline across all approximations, we retain $\tilde{Z}_\Delta$ explicitly in every step, akin to the canonical choice of $\tilde{Z}_\Delta=1$.

IV. RG-CONSISTENT MEAN-FIELD APPROXIMATION

We now adopt an alternative perspective on the mean-field approximation, which is based on the functional renormalization group (FRG). First, we demonstrate how the FRG framework reproduces the regMFA. We then use this approach to construct RG-consistent (RGC) approximations, with a particular focus on the treatment of medium divergences. This leads to alternative forms of the effective potential, which we compare with the renormalized approach in Secs. V and VI.

A. FRG and MFA

The FRG is rooted in the Wilsonian formulation of the renormalization group in quantum field theory. The Wilsonian coarse-graining procedure is captured by a functional differential equation for an effective action. In this work, we employ the Wetterich equation [18], where the central object is the scale-dependent one-particle irreducible effective action Γ_k with the infrared (IR) cutoff scale k. For a purely fermionic theory, the Wetterich equation takes the form

$$\partial_t\Gamma_k=-\frac{1}{2}\mathrm{Tr}[(\Gamma_k^{(2)}+R_k)^{-1}\partial_tR_k], \tag{26}$$

where $\partial_t=k\partial_k$ denotes the derivative with respect to the dimensionless scale $t=\ln(k/\Lambda)$ with the UV cutoff scale Λ. In Eq. (26), $\Gamma_k^{(2)}$ denotes the full two-point function (i.e., the inverse full propagator) for the fermion fields. With the superfield $\Psi^{\mathsf{T}}=(q^{\mathsf{T}},\bar{q})$, it is defined in momentum space as

$$\Gamma_k^{(2)} = \frac{\delta^2 \Gamma_k}{\delta \Psi^{\mathsf{T}}(p) \delta \Psi(p)}. \tag{27}$$

The trace Tr in Eq. (26) runs over all relevant spaces, including momentum, color, flavor, and Dirac spaces on which the fermionic fields are defined. The regulator function $R_k(p)$ implements the Wilsonian coarse-graining procedure within the path-integral formulation by acting as a scale-dependent mass term. In this work, we employ the sharp three-dimensional regulator function for fermions [38,39], given by

$$R_k(p) = i\vec{p}\left(\frac{1}{\theta(\vec{p}^2 - k^2)} - 1\right), \tag{28}$$

which renders momentum modes with $p < k$ infinitely massive, while vanishing for $p > k$. This choice is particularly convenient, as it leads to an expression for the effective potential that coincides with the result obtained in the regMFA using a three-momentum cutoff, as shown in Eq. (3).

Solving the Wetterich equation Eq. (26) with the initial condition Γ_Λ at the UV scale $k = \Lambda$ yields the full effective action $\Gamma = \Gamma_{k=0}$ in the infrared limit. In general, Γ_k admits an infinite expansion in terms of effective operators, rendering the exact treatment of the effective action intractable without suitable truncations.

To recover the MFA results, we employ the following ansatz for the effective action of the quark-meson-diquark model in Euclidean space

$$\Gamma_k = \int_0^\beta dx_4 \int d^3x \Big\{ \bar{q}[\not{\partial} - \mu\gamma_4 + g_\phi \sigma] q + \frac{1}{2} g_\Delta \Delta (\bar{q}\gamma_5 \tau_2 i\epsilon_3 C \bar{q}^{\mathsf{T}} - q^{\mathsf{T}} C \gamma_5 \tau_2 i \epsilon_3 q) + \Omega_k^{\text{eff}} \Big\}, \tag{29}$$

where σ and Δ denote the homogeneous background fields associated with the scalar σ and the diquark Δ_3 channels, respectively. The scale-dependent effective potential $\Omega_k^{\text{eff}}(\sigma, \Delta; T, \mu)$ is treated as a general function of σ and Δ and depends on T and μ, generally. In the infrared limit, it corresponds to the thermodynamic effective potential

$$\Omega^{\text{eff}} \equiv \frac{1}{\beta V} \Gamma_{k=0} = \Omega_{k=0}^{\text{eff}}, \tag{30}$$

where V denotes the three-dimensional spatial volume. At the UV scale $k = \Lambda$, and for a given T and μ, we initialize the flow with the polynomial form

$$\Omega_{k=\Lambda}^{\text{eff}}(\sigma, \Delta; T, \mu) = U(\sigma^2, \Delta^2) - c\sigma - 4Z_\Delta \mu^2 \Delta^2 \equiv \Omega_{\text{init}}^{\text{eff}}(\sigma, \Delta; \mu), \tag{31}$$

which is consistent with the classical action of the quark-meson-diquark model in Eq. (1) and depends only on μ.

Next, we observe that for the truncation Eq. (29), the inverse two-point function is independent of the RG scale k and coincides with the second derivative of the classical action given in Eq. (1),

$$\Gamma_k^{(2)} = S^{(2)}, \tag{32}$$

where $S^{(2)}$ is defined analogously to Eq. (27). This identification lies at the heart of the mean-field approximation and allows the Wetterich equation to be rewritten as

$$\begin{aligned} \partial_k \Gamma_k &= -\frac{1}{2} \text{Tr}[(S^{(2)} + R_k)^{-1} \partial_k R_k] \\ &= -\frac{1}{2} \partial_k \text{Tr}[\ln (S^{(2)} + R_k)]. \end{aligned} \tag{33}$$

With the truncation Eq. (29), we obtain the flow equation for the effective potential

$$\partial_k \Omega_k^{\text{eff}}(\sigma, \Delta; T, \mu) = \partial_k f_k(\sigma, \Delta; T, \mu), \tag{34}$$

where we introduce the shorthand notation

$$f_k = -\frac{1}{\beta V} \frac{1}{2} \text{Tr}[\ln (S^{(2)} + R_k)]. \tag{35}$$

Evaluating the trace over flavor, color and Dirac indices, and performing the Matsubara sums in Eq. (35), one obtains

$$f_k(\sigma, \Delta; T, \mu) = -L_k(m_q, \Delta_{\text{gap}}; T, \mu), \tag{36}$$

where $L_k(m_q, \Delta_{\text{gap}}; T, \mu)$ is defined in Eq. (4).

To derive the infrared mean-field potential, we integrate Eq. (34) from $k = \Lambda$ to $k = 0$ and recover the regularized effective potential Eq. (3)

$$\Omega_{\text{reg}}^{\text{eff}}(\sigma, \Delta; T, \mu) = \Omega_\Lambda^{\text{eff}}(\sigma, \Delta; T, \mu) + L_\Lambda(m_q, \Delta_{\text{gap}}; T, \mu), \tag{37}$$

where we have used $L_{k=0}(m_q, \Delta_{\text{gap}}; T, \mu) = 0$.

Lastly, we remark that the mean-field flow Eq. (33) with the sharp momentum regulator Eq. (28) can be understood as a mapping that directly relates the RG scale k to the UV cutoff scale Λ. With this in mind, one can alternatively derive the scale dependence of the couplings, the β-functions, directly from the Wetterich equation by solving their associated flow equations. This procedure reproduces the scale dependency of the couplings in Eqs. (11) to (16) and is explicitly demonstrated in Appendix B.

In the following, we extend this analysis by utilizing the FRG flow to eliminate cutoff artifacts, building on the concept of RG-consistency [10]. In particular, we focus on

the treatment of medium divergences within this framework.

B. RG-consistency of the QMD model

The concept of RG-consistency was introduced in Ref. [10] and has recently been discussed in the context of the $N_f = 3$ NJL model in Ref. [17]. It requires that the full quantum effective action Γ remains independent of the explicit cutoff dependence of Γ_Λ,

$$\Lambda \frac{\mathrm{d}\Gamma}{\mathrm{d}\Lambda} = 0. \tag{38}$$

In practice, however, this property is not automatically guaranteed if external scales of the theory, such as the temperature or the quark chemical potential, approach the cutoff scale Λ.

This issue can be resolved using the FRG. The underlying idea is most transparently illustrated in the context of the NJL model [17]. Suppose the initial conditions are originally specified by the effective potential $\Omega^{\mathrm{eff}}_{\Lambda'}(\sigma, \Delta; T, \mu)$ at some fixed scale Λ', for instance obtained via a vacuum fit at that cutoff. By formally integrating the flow in vacuum upward to a higher scale $k = \Lambda > \Lambda'$, one can construct a modified initial condition $\Omega^{\mathrm{eff}}_{\Lambda}(\sigma, \Delta; T, \mu)$, that reproduces the same infrared effective potential in vacuum. However, flowing downward from $k = \Lambda$ to $k = 0$ yields an RG-consistent effective potential $\Omega^{\mathrm{eff}}_{k=0}(\sigma, \Delta; T, \mu)$ even in the presence of finite external scales, provided that Λ is much larger than these scales (e.g., $\Lambda \gg T, \mu$).

For the QMD model, the general strategy remains the same. However, a small difference arises: the effective potential at the initial UV scale, denoted henceforth as Λ', includes an explicitly μ-dependent term originating from the diquark kinetic term, see Eq. (31). However, in the FRG MFA, this term does not affect the behavior of the medium divergence, and hence its treatment remains similar to the NJL model.

From this, the RG-consistent initial effective potential at $k = \Lambda$, $\Omega^{\mathrm{eff}}_{\mathrm{rgc},\Lambda}$, can be constructed, starting with the initial potential $\Omega^{\mathrm{eff}}_{\mathrm{init}}$ defined in Eq. (31), by integrating the mean-field flow, Eq. (34), upward from Λ' to Λ,

$$\Omega^{\mathrm{eff}}_{\mathrm{rgc},\Lambda}(\sigma, \Delta; \mu) = \Omega^{\mathrm{eff}}_{\mathrm{init}}(\sigma, \Delta; \mu) + \mathcal{F}_{\Lambda' \to \Lambda}(\sigma, \Delta; 0, 0), \tag{39}$$

with the flow integral

$$\mathcal{F}_{\Lambda' \to \Lambda}(\sigma, \Delta; T, \mu) = \int_{\Lambda'}^{\Lambda} dk \partial_k f_k(\sigma, \Delta; T, \mu) \tag{40}$$

$$= L_{\Lambda'}(m_q, \Delta_{\mathrm{gap}}; T, \mu) - L_{\Lambda}(m_q, \Delta_{\mathrm{gap}}; T, \mu). \tag{41}$$

As indicated, the flow and loop contributions defined in Eqs. (35) and (36) and consequently the flow integral $\mathcal{F}$ generally depend on T and μ. However, in Eq. (39) the UV effective potential at $k = \Lambda$ is connected to the UV effective potential at $k = \Lambda'$ via a flow contribution in vacuum ($T = \mu = 0$), in accordance with the general idea outlined above.

The infrared effective potential at arbitrary T and μ is then found by integrating the flow from $k = \Lambda$ to $k = 0$,

$$\Omega^{\mathrm{eff}}_{\mathrm{rgc}}(\sigma, \Delta; T, \mu) = \Omega^{\mathrm{eff}}_{\mathrm{rgc},\Lambda}(\sigma, \Delta; \mu) + \mathcal{F}_{\Lambda \to 0}(\sigma, \Delta; T, \mu). \tag{42}$$

As we will discuss next, the initial conditions at $k = \Lambda$, Eq. (39), need to be modified further because of medium divergences. However, Eq. (42) remains valid for all RGC schemes introduced in this context.

C. Treatment of medium divergences

For the QMD model, the procedure outlined above removes possible cutoff artifacts at finite T, but not at finite μ. This is due to the presence of the medium divergence in Eq. (9). Since the modified initial condition in Eq. (39) contains only vacuum flow contributions, it is insensitive to divergences that vanish when $\mu = 0$.[5]

To address this issue, the solution originally proposed in Ref. [10] was to perform a Taylor expansion of the upward flow in powers of μ and add this term to the right-hand side of Eq. (39)

$$\Omega^{\mathrm{eff}}_{\sigma\Delta,\Lambda}(\sigma, \Delta; \mu) = \Omega^{\mathrm{eff}}_{\mathrm{init}}(\sigma, \Delta; \mu) + \mathcal{F}_{\Lambda' \to \Lambda}(\sigma, \Delta; 0, 0) + \frac{\mu^2}{2} (\partial_\mu^2 \mathcal{F}_{\Lambda' \to \Lambda}(\sigma, \Delta; 0, \mu))\Big|_{\mu=0}. \tag{43}$$

The RG-consistent approximation to the effective potential is then again obtained by integrating the flow from $k = \Lambda$ to $k = 0$, as given in Eq. (42).

In Eq. (43), we implicitly allowed the last term to depend on the background fields σ and Δ. For this reason we refer to this scheme as the $\sigma\Delta$ scheme. Note however that this dependence is *not* determined by the requirement of RG consistency; any counterterm that removes the logarithmic medium divergence $\propto \mu^2\Delta^2 \ln(\Lambda)$ is admissible. Consequently, there exists an intrinsic scheme ambiguity in the construction of an RG-consistent mean-field potential.

An illustration of this ambiguity was given in Ref. [17]. In addition to the $\sigma\Delta$ scheme (which was called the *massive scheme* in Ref. [17]) the authors proposed a *minimal scheme* that takes advantage of the fact that the divergent term depends only on $\mu^2\Delta^2$. By setting $\sigma = 0$ and expanding only to second order in μ^2 and Δ^2, one obtains the modified initial condition

[5]Here, we treat the diquark wave function renormalization Z_Δ as independent of the cutoff scale. In the renormalized approach discussed in Sec. III, it is exactly the running of this term that cancels the medium divergence.

$$\Omega^{\text{eff}}_{\text{min},\Lambda}(\sigma,\Delta;\mu) = \Omega^{\text{eff}}_{\text{init}}(\sigma,\Delta;\mu) + \mathcal{F}_{\Lambda'\to\Lambda}(\sigma,\Delta;0,0) + \frac{1}{4}\mu^2\Delta^2(\partial_\mu^2\partial_\Delta^2\mathcal{F}_{\Lambda'\to\Lambda}(0,\Delta;0,\mu))\Big|_{\mu=\Delta=0}, \tag{44}$$

which removes the logarithmic divergence without introducing any additional field-dependent counterterms. Again, the RG-consistent effective potential is obtained by integrating the flow from $k=\Lambda$ to $k=0$ as in Eq. (42).

We note that the last term in Eq. (44) can be combined with the Z_Δ-term to define a scale-dependent wave-function renormalization constant $Z_\Delta(k) \propto \partial_\mu^2\partial_\Delta^2\Omega_k|_{\Delta=\mu=0}$. In fact, the minimal prescription reproduces exactly the running of Z_Δ that appears in the fully renormalized model, see Sec. III. In this sense it is the *closest* RG-consistent analog of the renormalized mean-field approximation known in the literature.

1. Vacuum matching scheme

The fact that the subtraction term of the *minimal scheme* defined in Eq. (44) can be reinterpreted as a scale–dependent wave function renormalization of the diquark field, makes this scheme particularly engaging. However, there is a drawback once one wishes to confront the RG–consistent framework with the standard (cutoff-)regularized mean-field model.

Using the definition of $\tilde{Z}_\Delta$ in Table I, and using Eq. (42) for the minimal scheme we find

$$\tilde{Z}_\Delta^{(\text{min})} = Z_\Delta - \frac{1}{16}(\partial_\mu^2\partial_\Delta^2\mathcal{F}_{\Lambda'\to\Lambda}(0,\Delta;0,\mu))\Big|_{\mu=\Delta=0} - \frac{1}{16}(\partial_\mu^2\partial_\Delta^2\mathcal{F}_{\Lambda\to 0}(\tilde{f}_\pi,\Delta;0,\mu))\Big|_{\mu=\Delta=0}, \tag{45}$$

whereas for the regularized model $\tilde{Z}_\Delta$ is obtained as

$$\tilde{Z}_\Delta^{(\text{reg})} = -\frac{1}{16}\partial_\mu^2\partial_\Delta^2\Omega^{\text{eff}}_{\text{reg}}\Big|_{\text{vac}} = Z_\Delta - \frac{1}{16}(\partial_\mu^2\partial_\Delta^2\mathcal{F}_{\Lambda'\to 0}(\tilde{f}_\pi,\Delta;0,\mu))\Big|_{\mu=\Delta=0}, \tag{46}$$

where we used Eqs. (3) and (40), remembering that the initial cutoff is now Λ' and $L_{k=0}=0$. Hence, taking the same Z_Δ, the two frameworks yield different results for $\tilde{Z}_\Delta$. Since we want to preserve $\tilde{Z}_\Delta$—as one of the vacuum parameters listed in Table I—across all approximations in order to enable a meaningful, parameter-synchronized comparison, this is a problem. In principle, this could be cured by readjusting the bare wave function renormalization constant Z_Δ in the minimal scheme, such that $\tilde{Z}_\Delta^{(\text{min})}$ becomes equal to $\tilde{Z}_\Delta^{(\text{reg})}$. On the other hand, it is one of the advantages of the RG-consistent approximation that cutoff artifacts present in the regularized model can be removed *without* changing the bare parameters (in contrast to full renormalization).

To resolve this issue, we introduce an alternative approach—the RGC vacuum matching scheme—which yields the same value for $\tilde{Z}_\Delta$ as for the regularized model while keeping Z_Δ (and all other bare parameters of the model) identical to the ones in the regularized model. In this scheme, the initial condition is fixed in vacuum, that is, evaluated at $\sigma=\tilde{f}_\pi$, where $\tilde{f}_\pi$ denotes the vacuum chiral condensate, and at $\Delta=0$. This leads to the following modified initial conditions

$$\Omega^{\text{eff}}_{\text{vm},\Lambda}(\sigma,\Delta;\mu) = \Omega^{\text{eff}}_{\text{init}}(\sigma,\Delta;\mu) + \mathcal{F}_{\Lambda'\to\Lambda}(\sigma,\Delta;0,0) + \frac{1}{4}\mu^2\Delta^2(\partial_\mu^2\partial_\Delta^2\mathcal{F}_{\Lambda'\to\Lambda}(\tilde{f}_\pi,\Delta;0,\mu))\Big|_{\mu=\Delta=0}. \tag{47}$$

This RGC scheme yields the same expression for $\tilde{Z}_\Delta$ as the regularized model

$$\begin{aligned}\tilde{Z}_\Delta^{(\text{vm})} &= Z_\Delta - \frac{1}{16}(\partial_\mu^2\partial_\Delta^2\mathcal{F}_{\Lambda'\to\Lambda}(\tilde{f}_\pi,\Delta;0,\mu))\Big|_{\mu=\Delta=0} - \frac{1}{16}(\partial_\mu^2\partial_\Delta^2\mathcal{F}_{\Lambda\to 0}(\tilde{f}_\pi,\Delta;0,\mu))\Big|_{\mu=\Delta=0}\\ &= Z_\Delta - \frac{1}{16}(\partial_\mu^2\partial_\Delta^2\mathcal{F}_{\Lambda'\to 0}(\tilde{f}_\pi,\Delta;0,\mu))\Big|_{\mu=\Delta=0}\\ &= \tilde{Z}_\Delta^{(\text{reg})}.\end{aligned} \tag{48}$$

We note that Eq. (47) is equivalent to Eq. (44) with a modified bare coupling Z_Δ. However, the vacuum matching scheme has the advantage that no explicit refit of Z_Δ is necessary in order to preserve the vacuum parameters of the regularized model.

From now on we will always assume that all bare parameters, including Z_Δ, in the RGC schemes are the same as the regularized model. For the minimal scheme this implies that $\tilde{Z}_\Delta$ will take a different vacuum value. A comparison of the results for the minimal and the vacuum matching schemes will therefore give us a hint on the importance of this parameter.

Note that the results obtained in our RG-consistent treatment differ in general from those of a renormalized mean-field model. This can be explained as follows. In the RGC treatment, the effective potential is initialized at a finite scale Λ' as a polynomial of fourth order in σ and Δ, see Eqs. (31) and (39). At any other scale $k\neq\Lambda'$, however, the quark loop generates infinitely many higher-order contributions to the effective potential beyond the initial fourth-order polynomial. This includes RG scales $k>\Lambda'$, and in particular the limit $k\to\infty$. In contrast, the renormalized model is defined by a potential with the same fourth-order polynomial form at $k\to\infty$. In this case, the RGC treatment and the renormalized model correspond to different UV effective actions. As a consequence, even if both models are fitted to the same set $\mathcal{P}_{\text{vac}}$ of vacuum

parameters listed in Eq. (17) and defined in Table I, all *other* correlators—such as the 6th-order derivatives of the effective potential—generally differ. In fact, even the fourth-order derivatives $\tilde{\lambda}_\phi = \frac{1}{6}(\partial_\sigma^4 \Omega^{\text{eff}})|_{\text{vac}}$ are not identical in both approaches because $\tilde{\lambda}_\phi$ does not belong to $\mathcal{P}_{\text{vac}}$.[6]

From the arguments above, it follows that the discrepancy increases as the UV cutoff Λ' is lowered. On the other hand, in the limit $\Lambda' \to \infty$, the UV effective action of the RGC treatment converges to that of the renormalized model. Accordingly, for sufficiently large Λ', the differences between the two approaches become negligible. However, as we will see in Sec. VI, even for a relatively low cutoff $\Lambda' = 600$ MeV, the prediction of the vacuum matching scheme and the renormalized approach are mostly similar. In the next Sec. V, we get back to this issue and analytically study the differences between these schemes in more details.

V. ANALYTICAL STUDIES

Before presenting the numerical results of our calculations, it is worthwhile to analytically examine certain aspects of the approximations employed in this work. Since the integrand in the gap equation or thermodynamic potential is typically sharply peaked at $p = \mu$, a common approximation, often found in the color superconductivity literature [40], is to restrict the momentum integration to a narrow window around the Fermi surface. This approximation simplifies the calculation while retaining the dominant physics of Cooper pairing—particularly in the weak-coupling regime, where the density of state is largest. For instance, in Ref. [41], a sharp regulator was imposed on the Fermi surface, yielding a finite and physically meaningful expression for the diquark gap

$$\bar{\Delta}_{\text{gap},0} = 2\omega \exp\left(-\frac{\pi^2}{2\lambda\mu^2}\right), \tag{49}$$

where $\bar{\Delta}_{\text{gap},0}$ denotes the diquark gap evaluated at $\sigma = 0$ and vanishing temperature. λ is the coupling constant, μ the chemical potential, and ω is the half of the size of the chosen cutoff around the Fermi surface. Another commonly employed approximation, used to obtain finite and cutoff-independent results, replaces parts of the integration measure in the three-momentum integral by the chemical potential and extracts it from the integral [25,42–44]

$$\int_0^\Lambda dp p^2 f(p) \quad \to \quad \mu^2 \int_0^\infty dp f(p). \tag{50}$$

Historically, such approximations were indispensable: without a proper renormalization procedure, loop integrals diverge as the ultraviolet integration bounds are taken to infinity. Moreover, a key benchmark in any superconducting framework is the BCS relation, which connects the critical temperature T_c to the zero-temperature pairing gap,

$$T_c = \frac{e^\gamma}{\pi} \bar{\Delta}_{\text{gap}}(T=0) \simeq 0.567 \bar{\Delta}_{\text{gap}}(T=0), \tag{51}$$

where $\gamma \simeq 0.5772$ is the Euler-Mascheroni constant. In weak-coupling QCD, an analogous relation has been derived for color superconductivity using similar approximations (see, e.g., Ref. [45]).

In contrast, our renormalized QMD model, as well as its RG-consistent treatment, allows us to evaluate the relevant integrals without such assumptions or encountering divergences. For massless quarks, i.e., $\sigma = 0$, at $T = 0$, we can solve the gap equation for the diquark condensate $\bar{\Delta}$ analytically, obtaining an explicit relation between $\bar{\Delta}$ and μ. Moreover, we derive a closed-form expression of the gap equation at the critical temperature T_c, corresponding to the vanishing gap, in terms of μ and $\bar{\Delta}_{\text{gap}}(T=0)$. With both quantities accessible analytically for arbitrary chemical potentials, we can explicitly test the BCS relation Eq. (51). We note that the case $\sigma = 0$ considered in the following section can alternatively be viewed as the mean-field solution of a quark-diquark model *without* mesons, see for example Refs. [10,46,47] for discussions on similar models.

In the remainder of this section we derive compact analytic formulas for the pressure, the asymptotic diquark gap, the speed of sound and for the BCS ratio $T_c/\bar{\Delta}_{\text{gap},0}$. In addition to the calculations for the renormalized model, we also study the asymptotic diquark gap for different RGC schemes, and identify which of the proposed approximations respects the BCS limit Eq. (51).

We note that some of our results for the renormalized model, Eqs. (57), (61) and (68), have also been derived in Ref. [11] using dimensional regularization, demonstrating the consistency between the two approaches. Moreover, the BCS relation was independently derived in a model similar to the QMD model in Ref. [48].

As before, and throughout the following, we use the overbar notation to distinguish the solution of the gap equation, $\bar{\Delta}$, from the general diquark field Δ. The subscript *gap* denotes the corresponding gap, obtained by multiplying Δ or $\bar{\Delta}$ with the diquark coupling g_Δ. Finally, the subscript 0 indicates that the quantity, $\bar{\Delta}$ or $\bar{\Delta}_{\text{gap}}$, is evaluated at $\sigma = 0$ and $T = 0$.

A. Pressure at $T = 0$

We start with the derivation of an analytical expression for the pressure in the renormalized model, which we compare with the Stefan-Boltzmann limit[7]

[6]Alternatively, we could have chosen $\tilde{\lambda}_\phi$ to be an element of $\mathcal{P}_{\text{vac}}$ instead of $\tilde{f}_\pi$. However, we prefer to fit all models to the pion decay constant, which has a more direct physical interpretation.

[7]Here we consider only quark degrees of freedom since mesons and diquarks do not contribute to the thermal pressure in mean-field approximation. In QCD there would be an additional gluonic contribution.

$$p_{\mathrm{SB}} = \frac{N_f N_c}{6}\left(\frac{7\pi^2}{30}T^4 + \mu^2 T^2 + \frac{\mu^4}{2\pi^2}\right). \tag{52}$$

For $\sigma = 0$ and $T = 0$, the loop and counterterm contribution Eq. (23) can be computed analytically

$$L_{\mathrm{ren}}(0,\Delta_{\mathrm{gap}};0,\mu) = \frac{1}{8\pi^2}\left\{3\Delta_{\mathrm{gap}}^4 - 12\Delta_{\mathrm{gap}}^2 m_{q,\mathrm{vac}}^2 - 4\mu^4 + 4\Delta_{\mathrm{gap}}^2(\Delta_{\mathrm{gap}}^2 - 4\mu^2)\ln\frac{m_{q,\mathrm{vac}}}{\Delta_{\mathrm{gap}}}\right\}, \tag{53}$$

which yields for the effective potential

$$\Omega_{\mathrm{ren}}^{\mathrm{eff}}(0,\Delta;0,\mu) = \left(\tilde{m}_\Delta^2 - \frac{1}{2}\tilde{\lambda}_{\mathrm{mix}}\tilde{f}_\pi^2\right)\Delta^2 - 4\tilde{Z}_\Delta\Delta^2\mu^2 + \tilde{\lambda}_\Delta\Delta^4 + L_{\mathrm{ren}}(0,\Delta_{\mathrm{gap}};0,\mu). \tag{54}$$

Following the procedure in Ref. [49] we use the gap equation, Eq. (25b), to replace $\tilde{m}_\Delta^2$. Then, using the definition of the pressure

$$p_{\mathrm{ren}}(T,\mu) = \Omega_{\mathrm{ren}}^{\mathrm{eff}}(\bar{\sigma},\bar{\Delta};0,0) - \Omega_{\mathrm{ren}}^{\mathrm{eff}}(\bar{\sigma},\bar{\Delta};T,\mu), \tag{55}$$

this yields the analytical form

$$\frac{p_{\mathrm{ren}}}{p_{\mathrm{SB}}} = 1 + 2\frac{\bar{\Delta}_{\mathrm{gap},0}^2}{\mu^2} + \frac{1}{4}\frac{\bar{\Delta}_{\mathrm{gap},0}^4}{\mu^4}\left(1 + \frac{8\pi^2}{g_\Delta^4}\tilde{\lambda}_\Delta + 4\ln\frac{m_{q,\mathrm{vac}}}{\bar{\Delta}_{\mathrm{gap},0}}\right). \tag{56}$$

We see that we recover the well-known first correction from the superconducting gap to the Stefan-Boltzmann pressure proportional to $\bar{\Delta}_{\mathrm{gap},0}^2/\mu^2$ [49,50]. Moreover, we observe from Eq. (56) that the quartic coupling only affects subleading contributions proportional to $\bar{\Delta}_{\mathrm{gap},0}^4$, which are negligible at high densities,

$$\frac{p}{p_{\mathrm{SB}}} = 1 + \frac{2\bar{\Delta}_{\mathrm{gap},0}^2}{\mu^2} + \mathcal{O}\left(\frac{\bar{\Delta}_{\mathrm{gap},0}^4}{\mu^4}\right). \tag{57}$$

We note that this expansion is a general feature of the model and remains valid, even when additional terms beyond the quartic coupling are included in the classical effective action.

B. Diquark condensate at $T = 0$

Next, we derive the diquark gap at vanishing temperature, which is obtained as the solution of the gap equation Eq. (25b). At zero temperature, the gap equation can be directly computed from Eq. (54) and yields

$$\left.\frac{\partial\Omega_{\mathrm{ren}}^{\mathrm{eff}}(\sigma,\Delta;0,\mu)}{\partial\Delta}\right|_{\substack{\sigma=0\\ \Delta=\bar{\Delta}_0}} = \bar{\Delta}_0\left[4\tilde{\lambda}_\Delta\bar{\Delta}_0^2 + 2\tilde{m}_\Delta^2 - \tilde{\lambda}_{\mathrm{mix}}\tilde{f}_\pi^2 - 8\tilde{Z}_\Delta\mu^2 + \frac{g_\Delta^2}{\pi^2}\left(\bar{\Delta}_{\mathrm{gap},0}^2 + 2\mu^2 - 3m_{q,\mathrm{vac}}^2 + 2(\bar{\Delta}_{\mathrm{gap},0}^2 - 2\mu^2)\ln\frac{m_{q,\mathrm{vac}}}{\bar{\Delta}_{\mathrm{gap},0}}\right)\right] = 0. \tag{58}$$

We note explicitly that $\bar{\Delta}_0 = 0$ is a trivial solution of Eq. (58). The nontrivial solution $\bar{\Delta}_0(\mu)$ to this equation is the inverse function of

$$\mu^2(\bar{\Delta}_0) = \frac{\mathcal{C}(\bar{\Delta}_0,\mathcal{P}_{\mathrm{vac}})}{2g_\Delta^2 - 8\pi^2\tilde{Z}_\Delta - 4g_\Delta^2\ln\frac{m_{q,\mathrm{vac}}}{\bar{\Delta}_{\mathrm{gap},0}}}, \tag{59}$$

where the numerator is defined as

$$\mathcal{C}(\bar{\Delta}_0,\mathcal{P}_{\mathrm{vac}}) \equiv -2\pi^2\tilde{m}_\Delta^2 + 3g_\Delta^2 m_{q,\mathrm{vac}}^2 + \pi^2\tilde{f}_\pi^2\tilde{\lambda}_{\mathrm{mix}} - 4\pi^2\bar{\Delta}_0^2\tilde{\lambda}_\Delta - \bar{\Delta}_{\mathrm{gap},0}^2 g_\Delta^2\left(1 + 2\ln\frac{m_{q,\mathrm{vac}}}{\bar{\Delta}_{\mathrm{gap},0}}\right), \tag{60}$$

and depends on the diquark condensate $\bar{\Delta}_0$ and the different vacuum parameters $\mathcal{P}_{\mathrm{vac}}$ defined in Eq. (17). Note that Eq. (59) is not generically monotonic and therefore not globally invertible. In practice, we restrict ourselves to the physical branch where the mapping is monotonic and the inversion is well-defined. Branches that would give $\mu^2 < 0$ are discarded as unphysical.

Because the denominator in Eq. (59) may vanish for specific values of $\bar{\Delta}_0$, a pole can appear in this expression. At this pole, μ diverges while $\bar{\Delta}_0$ remains finite. This defines the asymptotic value of the diquark condensate,

$$\lim_{\mu\to\infty}\bar{\Delta}_{\mathrm{gap}}^{(\mathrm{ren})} = m_{q,\mathrm{vac}}\exp\left(-\frac{1}{2} + \frac{2\pi^2}{g_\Delta^2}\tilde{Z}_\Delta\right), \tag{61}$$

which coincides with the result of Ref. [11] if we adopt their choice $\tilde{Z}_\Delta = 1$. The explicit dependence on $\tilde{Z}_\Delta$ in our expression is a consequence of our treatment of the diquark wave function renormalization. If we instead worked with the canonically normalized diquark field, $\Delta \to \tilde{Z}_\Delta^{-1/2}\Delta$, then the quantity $g_\Delta^2/\tilde{Z}_\Delta$ would correspond to the infrared Yukawa coupling of the canonically normalized field. See the last paragraph of Sec. III B for more details. Contrary to expectations from QCD [7,24,25,51], the QMD model predicts a finite asymptotic limit for Δ as $\mu \to \infty$ in MFA. Among the parameters of the model only the infrared

diquark coupling $g_\Delta/\tilde{Z}_\Delta$ and the vacuum quark mass $m_{q,\mathrm{vac}}$ determine the asymptotic value of the diquark gap.

Note that the numerator of Eq. (59) is nonzero at the pole solution for the parameters chosen here. However, one could select parameters such that μ^2 becomes negative, making μ imaginary and hence nonphysical for some $\Delta < \lim_{\mu\to\infty} \bar{\Delta}^{(\mathrm{ren})}_{\mathrm{gap}}$. In this case, diquark condensation might start at a large value already when $\mu = 0$ and then decrease to the asymptotic value as μ grows. While this behavior is mathematically admissible for certain parameter choices, we do not consider it to be physically meaningful.

A similar analysis for the RGC minimal scheme gives

$$\lim_{\mu\to\infty} \bar{\Delta}^{(\mathrm{min})}_{\mathrm{gap}} = 2\Lambda' \exp\left(-\frac{3}{2} + \frac{2\pi^2}{g_\Delta^2} Z_\Delta\right), \tag{62}$$

which resembles the $\mu \to \infty$ limit of Eq. (49), as it is proportional to the cutoff scale Λ'. In contrast, the RGC vacuum matching scheme yields (see Appendix D for details)

$$\lim_{\mu\to\infty} \bar{\Delta}^{(\mathrm{vm})}_{\mathrm{gap}} = m_{q,\mathrm{vac}} \exp\left\{-\frac{1}{2} + \frac{2\pi^2}{g_\Delta^2} Z_\Delta - \frac{\Lambda'}{\sqrt{\Lambda'^2 + m_{q,\mathrm{vac}}^2}} + \operatorname{artanh} \frac{\Lambda'}{\sqrt{\Lambda'^2 + m_{q,\mathrm{vac}}^2}}\right\}, \tag{63}$$

which then by using the relation for $\tilde{Z}_\Delta$ from Eq. (48),

$$\tilde{Z}_\Delta = Z_\Delta - \frac{g_\Delta^2}{2\pi^2}\left\{\frac{\Lambda'}{\sqrt{\Lambda'^2 + m_{q,\mathrm{vac}}^2}} - \operatorname{artanh} \frac{\Lambda'}{\sqrt{\Lambda'^2 + m_{q,\mathrm{vac}}^2}}\right\}, \tag{64}$$

reproduces the expression given in Eq. (61),

$$\lim_{\mu\to\infty} \bar{\Delta}^{(\mathrm{vm})}_{\mathrm{gap}} = \lim_{\mu\to\infty} \bar{\Delta}^{(\mathrm{ren})}_{\mathrm{gap}}. \tag{65}$$

C. Speed of sound at $T = 0$

From the pressure, the squared speed of sound at constant specific entropy s/n (with entropy $s = \frac{dp}{dT}$ and number density $n = \frac{dp}{d\mu}$) can be computed directly as

$$c_s^2 = \left.\frac{dp}{d\epsilon}\right|_{s/n} = \frac{dp}{d\mu}\left(\mu \frac{d^2 p}{d\mu^2}\right)^{-1}, \tag{66}$$

where the last equality holds only at zero temperature, $T = 0$. Using the fact that the diquark condensate saturates to a constant value as $\mu \to \infty$, and employing Eq. (56), we derive the exact expression

$$c_s^2 = \frac{\mu^2 + \bar{\Delta}^2_{\mathrm{gap},0}}{3\mu^2 + \bar{\Delta}^2_{\mathrm{gap},0}}, \tag{67}$$

where we have assumed that the gap has reached its asymptotic value and neglected its μ dependency. Expanding in powers of $\bar{\Delta}^2_{\mathrm{gap},0}/\mu^2$, we find

$$c_s^2 = \frac{1}{3} + \frac{2}{9}\frac{\bar{\Delta}^2_{\mathrm{gap},0}}{\mu^2} + \mathcal{O}\left(\frac{\bar{\Delta}^4_{\mathrm{gap},0}}{\mu^4}\right), \tag{68}$$

which shows that the squared speed of sound will always approach the conformal limit $c_s^2 = 1/3$ from above. This stands in contrast to predictions from perturbative QCD [52–55]. However, once improvements to the perturbative expansion are implemented, either through resummation techniques [56] or by incorporating the pairing gap [51,57,58], the situation becomes less clear.

D. The critical temperature

Next we derive the critical temperature. For this purpose we follow the procedure that leads to the derivation of the BCS relation. With $\sigma = 0$, we consider the gap equations for the diquark field at $T = 0$ and at $T = T_c$ (with $\Delta = 0$),

$$\left.\frac{\partial \Omega^{\mathrm{eff}}_{\mathrm{ren}}(\sigma, \Delta; 0, \mu)}{\partial \Delta}\right|_{\substack{\sigma=0 \\ \Delta=\bar{\Delta}_0}} = 0, \tag{69a}$$

$$\left.\frac{\partial \Omega^{\mathrm{eff}}_{\mathrm{ren}}(\sigma, \Delta; T_c, \mu)}{\partial \Delta}\right|_{\substack{\sigma=0 \\ \Delta=0}} = 0. \tag{69b}$$

To remove the trivial solution $\Delta = 0$, we rewrite the gap equations noting that $\frac{\partial}{\partial \Delta} = 2\Delta \frac{\partial}{\partial(\Delta^2)}$, and then drop the overall factor of Δ.

Thus, the relevant conditions become

$$\left.\frac{\partial \Omega^{\mathrm{eff}}_{\mathrm{ren}}(\sigma, \Delta; 0, \mu)}{\partial (\Delta^2)}\right|_{\substack{\sigma=0 \\ \Delta=\bar{\Delta}_0}} = 0, \tag{70a}$$

$$\left.\frac{\partial \Omega^{\mathrm{eff}}_{\mathrm{ren}}(\sigma, \Delta; T_c, \mu)}{\partial (\Delta^2)}\right|_{\substack{\sigma=0 \\ \Delta=0}} = 0. \tag{70b}$$

Taking the difference of these equations leads to

$$\left.\frac{\partial\Omega^{\mathrm{eff}}_{\mathrm{ren}}(\sigma,\Delta;0,\mu)}{\partial(\Delta^2)}\right|_{\substack{\sigma=0\\ \Delta=\bar{\Delta}_0}} - \left.\frac{\partial\Omega^{\mathrm{eff}}_{\mathrm{ren}}(\sigma,\Delta;T_c,\mu)}{\partial(\Delta^2)}\right|_{\substack{\sigma=0\\ \Delta=0}}$$
$$= 2\tilde{\lambda}_\Delta\bar{\Delta}_0^2 - \frac{g_\Delta^2}{6\pi^2}\left[2\pi^2T_c^2 + 3\bar{\Delta}_{\mathrm{gap},0}^2\left(2\ln\frac{\bar{\Delta}_{\mathrm{gap},0}}{m_{q,\mathrm{vac}}} - 1\right) + 12\mu^2\left(\ln\frac{\pi T_c}{\bar{\Delta}_{\mathrm{gap},0}} - \gamma\right)\right] = 0, \tag{71}$$

which can be solved to obtain $T_c(\bar{\Delta}_0,\mu)$ as

$$T_c^2(\bar{\Delta}_0,\mu) = \frac{3\mu^2}{\pi^2}W\left(\frac{\bar{\Delta}_{\mathrm{gap},0}^2}{3\mu^2}\exp\left[2\gamma + \frac{\bar{\Delta}_{\mathrm{gap},0}^2}{\mu^2}\left(\frac{1}{2} + \frac{2\pi^2}{g_\Delta^4}\tilde{\lambda}_\Delta - \ln\frac{\bar{\Delta}_{\mathrm{gap},0}}{m_{q,\mathrm{vac}}}\right)\right]\right), \tag{72}$$

where W denotes the Lambert W-function (for more details see Appendix C). Furthermore, we obtain an explicit analytical relation between T_c and μ by following the procedure detailed in Appendix C. We get

$$T_c^2(\mu) = \frac{3\mu^2}{\pi^2}W\left(\frac{m_{q,\mathrm{vac}}^2}{3\mu^2}\exp\left[-1 + 2\gamma + \frac{4\pi^2\tilde{Z}_\Delta}{g_\Delta^2} + \frac{1}{2\mu^2}\left(\left(3 + \frac{\pi^2\tilde{\lambda}_{\mathrm{mix}}}{g_\Delta^2 g_\sigma^2}\right)m_{q,\mathrm{vac}}^2 - \frac{2\pi^2}{g_\Delta^2}\tilde{m}_\Delta^2\right)\right]\right). \tag{73}$$

The weak-coupling regime is characterized by a vanishing ratio $\bar{\Delta}_{\mathrm{gap},0}/\mu$, which can be reached in two distinct ways: either by taking $\bar{\Delta}_{\mathrm{gap},0}\to 0$, or by sending $\mu\to\infty$. Using the relation Eq. (72) and taking the $\bar{\Delta}_{\mathrm{gap},0}\to 0$ limit of $T_c/\bar{\Delta}_{\mathrm{gap},0}$, we recover the standard BCS ratio,

$$\lim_{\bar{\Delta}_{\mathrm{gap},0}\to 0}\frac{T_c}{\bar{\Delta}_{\mathrm{gap},0}} = \frac{e^\gamma}{\pi}, \tag{74}$$

where we used $\lim_{x\to 0}W(x)/x = 1$. Taking the limit $\mu\to\infty$ of Eq. (73) and using Eq. (61) yields

$$\lim_{\mu\to\infty}T_c = \frac{\mathrm{e}^\gamma}{\pi}\lim_{\mu\to\infty}\bar{\Delta}_{\mathrm{gap},0}, \tag{75}$$

confirming the BCS relation as well. Note, however, that the limits in Eqs. (74) and (75) are reached along different trajectories in parameter space and therefore do not coincide in general. We will come back to this point in Sec. VI C.

Similar expressions to Eqs. (72) and (73) can be derived for all RGC schemes. These results are provided in Appendix D. Eventually, in the limit of $\bar{\Delta}_{\mathrm{gap},0}\to 0$, the BCS relation Eq. (74) is obtained for all the RGC schemes studied in this work. However, in the limit of $\mu\to\infty$ Eq. (75), the BCS relation is only realized for the RGC minimal scheme and the vacuum matching scheme but not in the $\sigma\Delta$ scheme. Particularly, due to the Δ-dependence of the wave function renormalization factor in this scheme, one cannot derive a closed-form expression for the diquark gap in the limit $\mu\to\infty$ (see Appendix D for a detailed analysis.). Nevertheless, in the $\sigma\Delta$ scheme the critical temperature can be expressed explicitly as a function of μ [see Eq. (D13)], and this expression coincides with the result obtained in the RGC-minimal scheme. Hence, for $\sigma = 0$ the two schemes yield identical 2SC phase boundaries. With the choice of $Z_\Delta = 0$, the asymptotic value for the critical temperature for these two schemes is shown to be directly connected to the scale Λ' via

$$\lim_{\mu\to\infty}T_c = \frac{e^\gamma}{\pi}\frac{2\Lambda'}{e^{\frac{3}{2}}}. \tag{76}$$

This holds even though Eq. (62) *is not* a solution of the $\sigma\Delta$ scheme's gap equation at $T = 0$. Hence, while for the $\sigma\Delta$ scheme, the standard BCS relation $T_c/\bar{\Delta}_{\mathrm{gap},0} = e^\gamma/\pi$ holds in the limit of $\bar{\Delta}_{\mathrm{gap},0}\to 0$, it does *not* hold as $\mu\to\infty$. Instead, the ratio $\lim_{\mu\to\infty}T_c/\bar{\Delta}_{\mathrm{gap},0}$ converges to a value that must be evaluated numerically and depends on the model parameters specific to this scheme.

E. Finite quark masses

In the analysis above, we have assumed vanishing quark masses, i.e., $m_q = g_\phi\sigma = 0$. This is correct in the chiral limit $c = 0$ above the chiral phase transition. In the following we argue that the results remain valid as $\mu\to\infty$, even for $c\neq 0$, i.e., away from the chiral limit. This assertion is supported by the following observations:

In the absence of diquark pairing ($\Delta = 0$), the chiral condensate σ tends to zero as μ approaches infinity. This aligns with the expectation that chiral symmetry is restored at high densities and can be readily verified by solving the gap equation Eq. (25a). Conversely, when the chiral condensate σ vanishes, the diquark gap Δ asymptotically approaches a finite constant. This behavior can be rigorously demonstrated away from the chiral limit as a simultaneous solution to the gap equations Eq. (25) in the limit $\mu\to\infty$. To establish this result, we applied the dominated convergence theorem to the gap equations, which justifies interchanging the limit and the integral in the gap equations. This rigorous treatment confirms that $\sigma\to 0$ and $\Delta\to\Delta_{\mathrm{asymp}}$ constitute the mutual solution to the gap equations at $T = 0$ as $\mu\to\infty$. Given the technical nature of this analysis, we refrain from presenting the detailed calculations here.

VI. NUMERICAL RESULTS

A. Fixing the vacuum parameters

In this section, we compare numerical results obtained from the different mean-field approximations to the QMD model introduced above. To ensure a meaningful

comparison, we fix the parameters such that all versions reproduce the same vacuum physics, ideally based on a common set of observables or quantities derived from QCD. Due to the limited availability of such data from either observations or first-principles calculations, we adopt values obtained within the regularized mean-field approximation (regMFA).

Our strategy proceeds as follows. As detailed below, we first fix the UV parameters of the regMFA model at a given cutoff scale Λ'. These parameters determine the vacuum quantities listed in Table I, which then serve to define the renormalized model, as outlined in Sec. III B. For the RGC schemes, by contrast, we directly adopt the UV parameters of the regMFA as input for the effective potential at the initial scale Λ'. In the *vacuum matching scheme*, the IR vacuum parameters are, by construction, identical to those obtained in the regMFA approach and, consequently, also to those of the renormalized model. In the minimal scheme, however, the resulting value of $\tilde{Z}_\Delta$ differs (see Sec. IV C), while the remaining vacuum parameters still coincide with the other schemes. In the regMFA and likewise in the RGC variants that retain an explicit wave function renormalization, the vacuum value of the diquark renormalization constant is $\tilde{Z}_\Delta \neq 1$. Because our renormalization conditions are imposed on *off-shell* correlators, the phenomenological input for the diquark sector is therefore not fixed by the physical pole mass. For that reason we keep $\tilde{Z}_\Delta$ explicit throughout, so every scheme can be compared on an equal footing.

Let us now explain in detail how the parameters of the regMFA model are fixed. Starting from the action Eq. (1), and recalling that the quark and meson wave function renormalizations do not enter directly in our equations, we are left with nine UV parameters: the bare meson and diquark masses m_ϕ and m_Δ, the Yukawa couplings g_ϕ and g_Δ, the quartic couplings λ_ϕ, λ_Δ and λ_{mix}, the explicit symmetry breaking parameter c, and the diquark wave function renormalization constant Z_Δ.

Among these, m_ϕ, g_ϕ, λ_ϕ and c belong to the quark-meson sector and can at least be partially constrained by vacuum observables such as the pion decay constant and the pion mass. In contrast, since diquarks do not exist as asymptotic states in vacuum, the diquark sector cannot directly be fixed from experimental observables. Here, we adopt values commonly used in the literature and compatible with typical theoretical expectations, see, e.g., Refs. [59–61] for estimates of the vacuum diquark mass.

In the absence of further constraints, we simplify the bosonic potential, Eq. (2), by setting $\lambda_\Delta = \lambda_{\mathrm{mix}} = 0$, yielding the reduced form

$$U(\phi^2, |\Delta|^2) = \frac{1}{2} m_\phi^2 \phi^2 + \frac{1}{4}\lambda_\phi \phi^4 + m_\Delta^2 |\Delta|^2. \quad (77)$$

Additionally, we set $Z_\Delta = 0$. This choice is motivated by the fact that in models without diquark kinetic terms, like the NJL model, there is no bare wave-function renormalization constant in the starting UV action, and therefore $Z_\Delta = 0$ would be realized at the initial scale Λ' in these models. In the QMD model, where diquark kinetic terms exist, other choices are possible. However, choosing $Z_\Delta = 0$ is particularly convenient for the RGC schemes, as it renders the UV initial conditions at μ-independent, see Eq. (31).

We are thus left with six nonvanishing UV parameters: m_ϕ, m_Δ, g_ϕ, g_Δ, λ_ϕ, and c. The diquark Yukawa coupling is set to $g_\Delta = 4.5$, which is not strongly constrained but yields a physically reasonable diquark gap at the onset of the color-superconducting phase (see VI B). To fix the remaining five parameters, we choose a UV cutoff $\Lambda' = 600$ MeV and fit the model to the following vacuum properties:

(1) *chiral condensate (pion decay constant)*

$$\tilde{f}_\pi = 92.4 \text{ MeV}, \quad (78)$$

(2) *pion mass*

$$m_\pi^2 = 2(\partial_{\sigma^2}\Omega)|_{\mathrm{vac}} = (137 \text{ MeV})^2, \quad (79)$$

(3) *sigma mass*

$$\tilde{m}_\sigma^2 = (560 \text{ MeV})^2, \quad (80)$$

(4) *quark mass*

$$m_{q,\mathrm{vac}} = g_\phi \tilde{f}_\pi = 300 \text{ MeV}, \quad (81)$$

(5) *diquark mass*

$$\tilde{m}_\Delta^2 = (600 \text{ MeV})^2. \quad (82)$$

The mesonic properties are taken from Ref. [62]. For the diquark mass, we assume it to be twice the quark mass, consistent with Refs. [59–61], provided the curvature mass of the diquark field is a good approximation to its pole mass.

The UV effective action parameters that reproduce these vacuum properties are then determined as

$$\begin{aligned} m_\phi^2 &= (951.5 \text{ MeV})^2, \\ m_\Delta^2 &= (959.2 \text{ MeV})^2, \\ \lambda_\phi &= -1.34, \\ c &= (120.7 \text{ MeV})^3, \\ g_\phi &= 3.25, \end{aligned}$$

together with our choice $g_\Delta = 4.5$ and $\lambda_\Delta = \lambda_{\mathrm{mix}} = Z_\Delta = 0$. With this set of bare parameters we can now calculate the six vacuum parameters Eq. (17) defined in Table I. The numerical values are listed in Table II. Note that this set of vacuum

TABLE II. Values for vacuum parameters.

Vacuum parameters	Value
$\tilde{f}_\pi$	92.4 MeV
$\tilde{m}_\sigma^2$	$(560\ \text{MeV})^2$
$\tilde{m}_\Delta^2$	$(600\ \text{MeV})^2$
$\tilde{\lambda}_{\text{mix}}$	−7.24
$\tilde{\lambda}_\Delta$	11.4
$\tilde{Z}_\Delta$	0.56

parameters has partial overlap with but is not identical to the vacuum quantities in Eqs. (78) to (82), which we used to fix the UV parameters. This is related to the fact that some of the UV parameters, like g_ϕ and c do not receive loop corrections in mean-field approximation but, of course, need to be fixed nonetheless (e.g., c via the pion mass). On the other hand, the vacuum parameters listed in Table I all receive loop corrections, so that λ_Δ, λ_{mix} and Z_Δ, which we set equal to 0 in the UV have nonzero vacuum values in the IR.

With these values at hand, we now have access to the renormalized effective potential. Notably, if the integration in the renormalized effective potential is carried out only up to a finite cutoff Λ' rather than to infinity, the resulting expression remains identical to that of the regularized potential. This property ensures consistency between the regularized and renormalized models.

For the RGC schemes, as explained above, we adopt the same UV parameters at the initial scale Λ'. This yields to identical IR vacuum parameters as those listed in Table II, with the exception of $\tilde{Z}_\Delta$ in the minimal scheme, which takes the value $\tilde{Z}_\Delta^{(\text{min})} = 0.39$. As we will see below, this deviation has consequences for some of the results.

In the following, we present numerical results for the different approximations discussed in this work. Details regarding the computational procedures and numerical implementation are provided in Appendix F.

B. Phase structure and thermodynamics

In Fig. 1, we present the QMD phase diagram obtained within the regularized and renormalized mean-field approximations, including all RGC schemes ($\sigma\Delta$, vacuum matching and minimal). Thin solid lines denote the chiral crossover, defined by the minimum of $\partial_\sigma^2\Omega$ at fixed μ, while thick solid lines indicate first-order phase transitions, where both chiral and diquark condensate are discontinuous. Dashed lines correspond to second-order diquark transitions, and critical endpoints are marked by dots. All approximations share the same qualitative structure: at low T and μ, the system resides in a chirally broken phase without diquark pairing; at low T and high μ, it enters the chirally restored, color-superconducting (2SC) phase; and at high T, chiral symmetry is restored with no diquark condensate. Quantitatively, however, significant differences

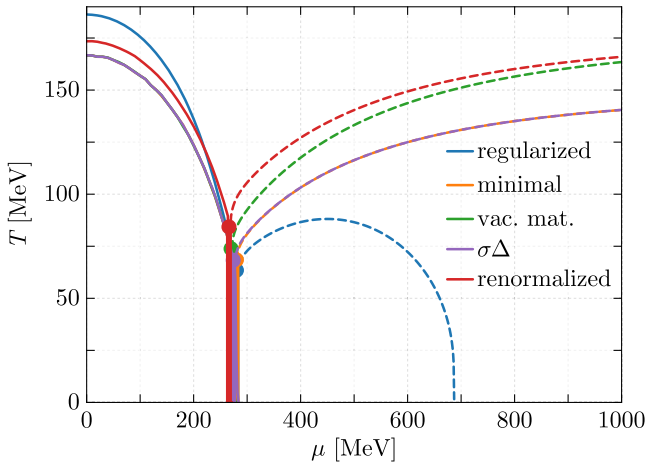

FIG. 1. Phase diagram corresponding to the different approximation schemes considered in this work. Thin solid lines denote crossover transitions of the chiral condensate, thick solid lines indicate first-order transitions for both the chiral and diquark condensates, and dashed lines represent second-order transitions for the diquark condensate. Dots mark the location of critical endpoints. Chiral crossover phase boundaries of all RGC schemes overlap. Note that the critical temperatures for the 2SC phase in the minimal and $\sigma\Delta$ schemes are identical. This is shown analytically for $\sigma = 0$, see Eq. (D13), and is confirmed here numerically, even away from the chiral limit.

emerge. In particular, the regMFA fails at large μ: its diquark boundary bends downward and eventually disappears, reflecting the absence of high-momentum contributions in the medium integrals. In contrast, all RGC schemes and the renormalized treatment maintain a 2SC phase up to arbitrarily large μ. Moreover, the regMFA overestimates the chiral crossover temperature at low μ, shifting the crossover line to higher T, and delaying the onset of the 2SC region to larger μ at low T.

To understand the origin of these differences, Fig. 2 shows the behavior of the condensates as functions of μ at $T = 0$ (left panel) and of T at $\mu = 0$ (right panel). At zero temperature, the diquark gap $\bar{\Delta}_{\text{gap}}$ in the regMFA initially increases but subsequently decreases and eventually vanishes at $\mu \simeq 686.5$ MeV. In contrast, the curves in the RGC schemes and the renormalized model exhibit the expected monotonic rise of $\bar{\Delta}_{\text{gap}}$, followed by saturation to constant values.

Similarly, the quark mass $\bar{m}_q = g_\phi\bar{\sigma}$ remains relatively large in the 2SC phase and tends toward a nonzero constant as $\mu \to \infty$ in the regMFA, while it asymptotically vanishes in the RGC and renormalized schemes. These differences can be traced back to the limited integration domain in the regMFA, which suppresses diquark pairing and consequently delays the 2SC onset. A detailed analysis for this behavior is provided in Appendix E.

Similarly, at $\mu = 0$, the regularized MFA restores chiral symmetry only at higher T, because the truncated thermal

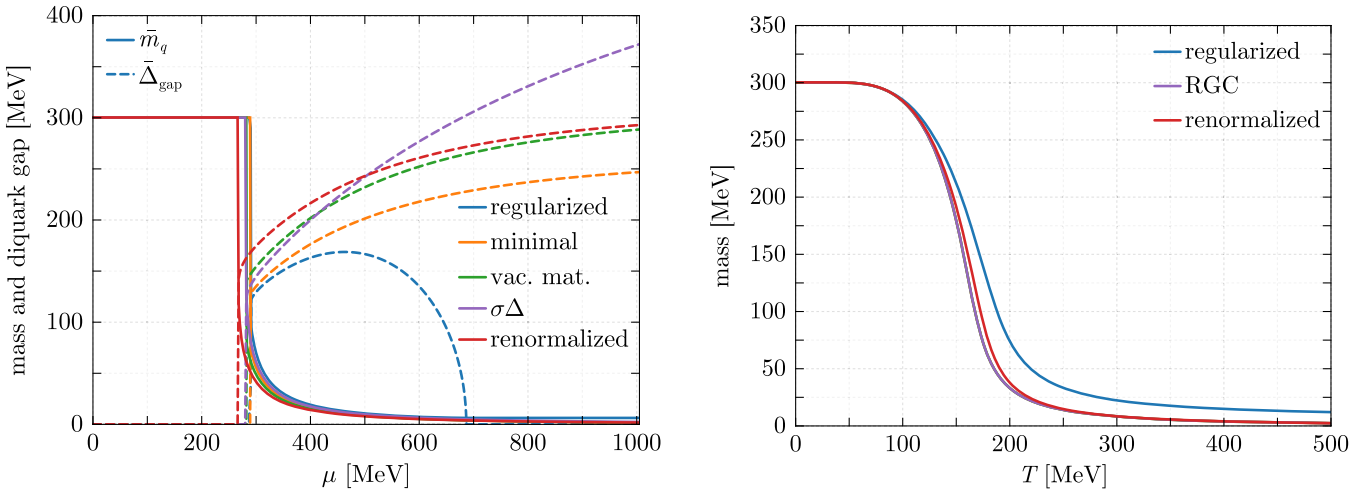

FIG. 2. Quark mass $\bar{m}_q = g_\phi \bar{\sigma}$ and diquark gap $\bar{\Delta}_{\rm gap} = g_\Delta \bar{\Delta}$ at $T = 0$ MeV (left), and quark mass at $\mu = 0$ (right) for the different approximations considered in this work. For $\mu = 0$ (right) the diquark gap always vanishes, $\bar{\Delta}_{\rm gap} = 0$, and is not shown. Also note that for $\mu = 0$ all RGC schemes are identical, while the renormalized model yields slightly different results.

integrals slow down the decrease of $\bar{m}_q$ and leave it nonzero even as $T \to \infty$, similar to what happens at $T = 0$ in the μ direction. In contrast, both the RGC and renormalized treatments drive $\bar{\sigma} \to 0$ at large T, giving a lower crossover temperature. Thus, in both the μ- and T-directions, the limited integration domains in the regMFA favor chiral condensate persistence, shifting the chiral-restoration crossover as well as the 2SC onset to higher external parameters when compared to the properly renormalized approaches.

We note that even for $\mu = 0$, the results of the renormalized and RGC approaches are not expected to be strictly identical by construction. The renormalized model is fixed by matching a finite set of vacuum observables, which are implemented through a limited number of derivatives of the effective potential with respect to σ at $\mu = 0$. As a consequence, some parameters that are not directly fixed by the vacuum matching conditions differ slightly between the two setups. For example, the mesonic self–interaction λ_ϕ (and similarly other higher–order couplings) takes different values in the RGC schemes compared to the renormalized model. These differences propagate into observables and lead to the small discrepancy visible in Fig. 2 (right).

In Sec. V and Appendices C and D, we derived closed-form expressions for $\mu(\bar{\Delta}_{\rm gap,0})$ and $T_c(\mu)$ in the limit $\sigma = 0$. To illustrate their accuracy, Fig. 3 compares these analytic results (solid curves) with the corresponding numerical results at physical quark masses (dashed lines taken from Figs. 1 and 2) for the renormalized model and for RGC

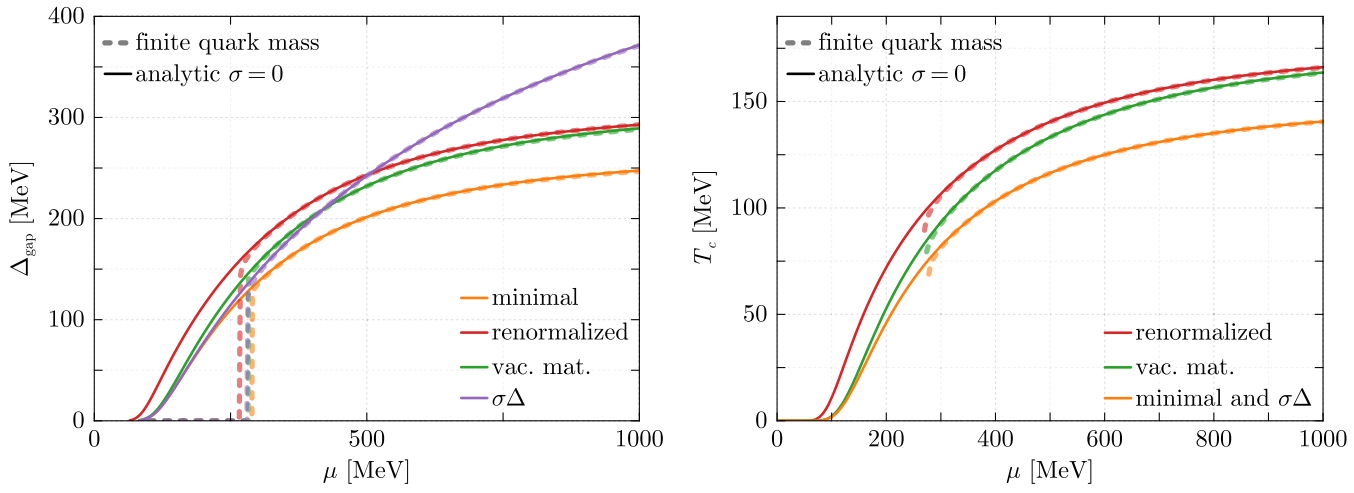

FIG. 3. Diquark gap $\Delta_{\rm gap}$ at $T = 0$ (left) and critical temperature T_c (right) against the chemical potential μ. Solid lines indicate closed-form expressions derived in the $\sigma = 0$ limit, while the dashed lines indicate results obtained numerically for the full solutions of the gap equation, including explicit chiral-symmetry breaking, see also Figs. 1 and 2.

schemes. In the left-hand panel, $\bar{\Delta}_{\mathrm{gap}}(T=0)$ is plotted against μ. In every case the numerical results merge with the chiral-limit curves almost immediately after diquark condensation sets in, indicating that at high density the dynamics is governed by quark-diquark properties while the chiral condensate (mesonic part) plays only a minor role. The same rapid convergence is visible in the right-hand panel for the 2SC phase boundaries $T_c(\mu)$.

The RGC vacuum matching and renormalized schemes differ only in their UV completion of the vacuum sector. Their small residual discrepancies arise from the choice of the RG matching scale Λ' and the specific set of vacuum operators retained at that scale. Both approaches nevertheless agree closely with each other, showing that once vacuum matching is imposed, the detailed structure of the UV effective action has only a minor impact on the medium physics. The RGC minimal scheme, however, deviates further due to its different value of $\tilde{Z}_\Delta$, and accordingly its diquark gap approaches a different constant at large μ: in the minimal RGC scheme one finds [see Eq. (62)]

$$\lim_{\mu\to\infty}\bar{\Delta}_{\mathrm{gap}}^{(\mathrm{min})}=267.8\ \mathrm{MeV},$$

whereas both the RGC vacuum matching and the renormalized schemes converge to [see Eqs. (61) and (65)]

$$\lim_{\mu\to\infty}\bar{\Delta}_{\mathrm{gap}}^{(\mathrm{vm})}=\lim_{\mu\to\infty}\bar{\Delta}_{\mathrm{gap}}^{(\mathrm{ren})}=315.2\ \mathrm{MeV},$$

consistent with the numerical results at $\mu=1000$ MeV in Fig. 2. Finally, the $\sigma\Delta$-scheme shows the most different behavior compared to the other schemes as the diquark gap grows much faster with μ. This is confirmed by the asymptotic value, which can be computed from the procedure outlined in Appendix D (see Eq. (D10) and also Fig. 6) to yield

$$\lim_{\mu\to\infty}\bar{\Delta}_{\mathrm{gap}}^{(\sigma\Delta)}=584.2\ \mathrm{MeV}.$$

Finally, as discussed in Sec. V D, the renormalized, as well as the minimal and the vacuum matching RGC schemes exhibit BCS scaling for the critical temperature T_c associated with the melting of the 2SC phase in the limit $\mu\to\infty$ as given by Eq. (75). Inserting the gaps at $\mu=1000$ MeV, one finds

$$T_c^{(\mathrm{min})}\approx 0.567\times 246.7\ \mathrm{MeV}\approx 139.9\ \mathrm{MeV},$$
$$T_c^{(\mathrm{vm})}\approx T_c^{(\mathrm{ren})}\approx 0.567\times 292.8\ \mathrm{MeV}\approx 166.0\ \mathrm{MeV},$$

in very good agreement with the 2SC boundaries in Fig. 1 already at $\mu=1000$ MeV

$$T_c^{(\mathrm{min})}=140.5\ \mathrm{MeV},\quad\text{and}$$
$$T_c^{(\mathrm{ren})}=166.0\ \mathrm{MeV}.$$

For the $\sigma\Delta$ scheme, we do not expect the BCS relation to hold. As shown analytically, the 2SC phase boundaries of the minimal scheme and the $\sigma\Delta$ scheme coincide for $\sigma=0$, and our results in Fig. 1 indicate that this agreement persists even away from the chiral limit. Despite the identical critical temperature curves in Figs. 1 and 2 reveals a pronounced difference in the diquark gap, confirming that the system is far from the BCS limit. Using the asymptotic critical temperature from Eq. (D14), $\lim_{\mu\to\infty}T_c^{(\sigma\Delta)}=151.8$ MeV, together with the asymptotic gap $\lim_{\mu\to\infty}\bar{\Delta}_{\mathrm{gap},0}^{(\sigma\Delta)}=584.2$ MeV, we obtain the ratio $\lim_{\mu\to\infty}\frac{T_c}{\Delta}=0.260$ for the chosen parameter set. Using this ratio, at $\mu=1000$ MeV, we find

$$T_c^{(\sigma\Delta)}\approx 0.260\times 373.6\ \mathrm{MeV}\approx 97.14\ \mathrm{MeV}.$$

This value does not match the computed 2SC boundary at $T_c^{(\sigma\Delta)}(\mu=1000\ \mathrm{MeV})=140.5$ MeV. The discrepancy arises because, in the $\sigma\Delta$ scheme, the diquark gap approaches its asymptotic limit much more slowly and saturates only at considerably larger μ (see Fig. 3 and also Sec. VI C).

In Fig. 4, we show the pressure p and the squared speed of sound c_s^2 at $T=0$ as functions of the chemical potential. As observed, the regMFA fails to approach the Stefan-Boltzmann limit for $\mu\to\infty$. Again, this deficiency is absent in the RGC and renormalized schemes, where the Stefan-Boltzmann limit is gradually attained in the high-density regime. For the speed of sound (right panel) we observe a peak exceeding the conformal limit $c_s^2=1/3$, which is a characteristic feature of models incorporating diquark condensation [11,12,33,63,64]. As discussed in Sec. V C, this quantity approaches the conformal value from above at large μ.

Additionally, in the regMFA the speed of sound exhibits an unphysical divergence at higher chemical potentials. This can be traced back to the behavior of the condensates in this approximation: as shown in Fig. 2, the diquark condensate vanishes and the chiral condensate $\bar{\sigma}$ tends toward a constant at large μ. Under these conditions, the regulated medium integrals lead to a linear increase of the pressure p with μ, while the energy density ϵ asymptotically saturates to a constant value (see Appendix E for details). Since the squared speed of sound is defined as $c_s^2=\frac{dp}{d\epsilon}$, this leads to $\frac{dp}{d\epsilon}\to\infty$, implying a divergent c_s^2 at high chemical potentials in the regMFA. This unphysical behavior of the speed of sound was discussed for the NJL model in Ref. [65].

We also compare the pressure and speed of sound to the weak coupling expansions, Eqs. (57) and (68), for two

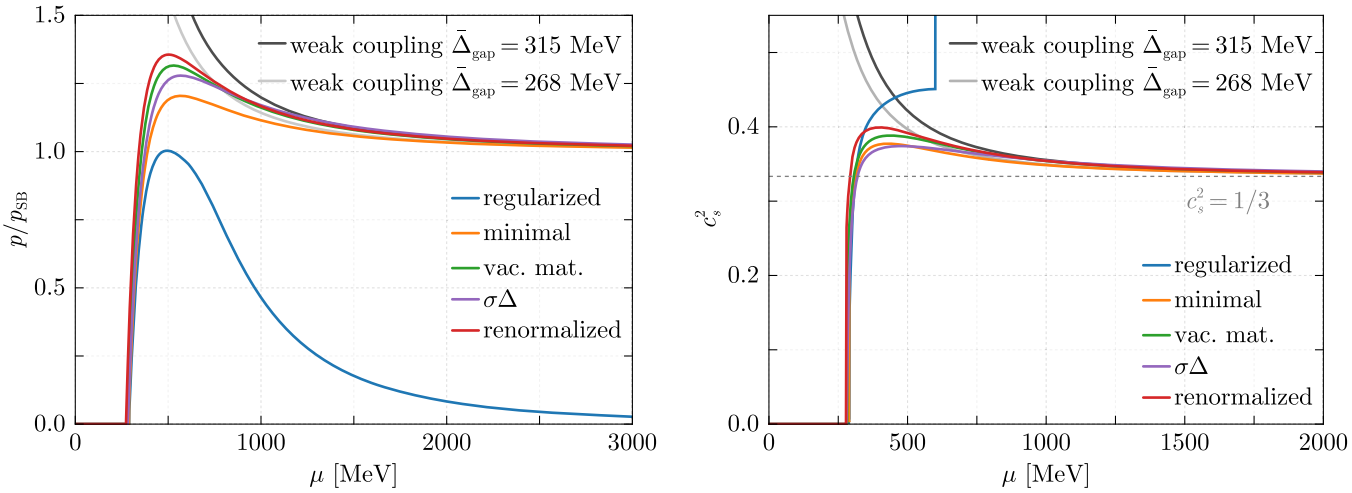

FIG. 4. Pressure p normalized to the Stefan-Boltzmann pressure $p_{\rm SB}$ (left) and squared speed of sound (right) as functions of μ at $T = 0$ MeV. The black and gray solid lines indicate the asymptotic behavior of the pressure, Eq. (57), and of the speed of sound, Eq. (68), expected from a weak-coupling expansion. The gray dashed line marks the conformal limit, $c_s^2 = 1/3$ (right).

constant diquark gap values corresponding to the asymptotic values for the minimal and renormalized schemes. At large densities $\mu \gtrsim 1.5$ GeV, we find a very good agreement between the weak-coupling expansion and the numerical results as already noted in Ref. [10].

The same cutoff artifacts that distort the phase diagram and the speed of sound at higher values of μ, are also visible in thermal observables. Because the regularized MFA omits high-momentum modes, its thermal pressure and entropy fall short of the Stefan-Boltzmann limits. Fig. 5 compares the entropy density of the five approximations with the SB limit

$$s_{\rm SB} = \frac{N_f N_c}{3}\left(\frac{7\pi^2}{15}T^3 + \mu^2 T\right). \tag{83}$$

For $\mu = 0$ (left panel) no diquark condensate is present, and after the chiral crossover the quark mass drops to nearly zero. One therefore expects $s/s_{\rm SB} \to 1$ at high temperature. All curves with RG consistent treatment and the renormalized curve meet this expectation, whereas the regMFA never reaches unity because the truncated momenta omit an increasing fraction of thermal modes as T grows.

The right panel shows the same ratio at $\mu = 450$ MeV, where a 2SC condensate persists up to the critical temperature. Below T_c the red–green quarks are gapped and exponentially suppressed, so only the ungapped blue quasiquarks contribute; consequently $s/s_{\rm SB} \simeq 1/3$, a limit reached by all five approximations. Above T_c the diquark gap vanishes and the quark mass is small; the RG-consistent

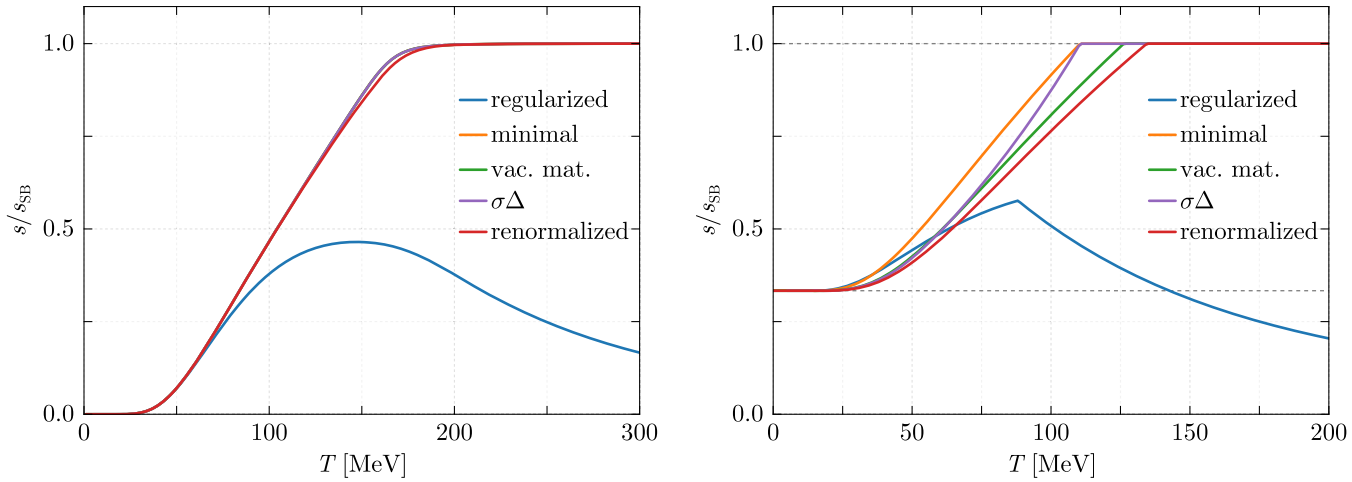

(a) $\mu = 0$ MeV (b) $\mu = 450$ MeV

FIG. 5. Entropy density s, normalized to the Stefan-Boltzmann entropy $s_{\rm SB}$ [Eq. (83)], as a function of T at $\mu = 0$ MeV (left) and $\mu = 450$ MeV (right). The horizontal dashed lines indicate $s/s_{\rm SB} = 1$ and $s/s_{\rm SB} = 1/3$.

and renormalized schemes therefore approach $s/s_{\mathrm{SB}} \to 1$. For temperatures near but below T_c, a linear increase in this ratio is observed in both the renormalized and RGC vacuum matching schemes, as well as in the minimal scheme, while this linear behavior is absent in the $\sigma\Delta$ scheme. The regularized MFA, however, breaks down once again, with the entropy ratio turning over and falling because the missing high-momentum thermal modes cannot be recovered by any further increase in T.

We emphasize that *all* thermodynamic observables tell the same story. Whether one probes along the temperature axis or along the chemical potential axis, the truncated integrals in the regularized MFA restrict the available phase space and, as a consequence, distort chiral and superconducting transitions as well as bulk quantities such as the entropy. By contrast, the RG-consistent and renormalized calculations, which integrate over the full momentum range, consistently recover the Stefan-Boltzmann limits and preserve the expected pattern of phase transitions throughout the entire (T, μ) plane.

C. Testing the BCS relation

With $\bar{\Delta}(T=0)$ and T_c at our hands, we can compare their ratio with the BCS result and also with the numerical results obtained away from the chiral limit. The results are shown in Fig. 6, where T_c is plotted as a function of the zero-temperature diquark gap, $\bar{\Delta}_{\mathrm{gap}}(T=0)$: the left panel of Fig. 6 shows the regularized model together with the RGC-minimal and vacuum matching schemes in comparison with the renormalized results, while the right panel displays the $\sigma\Delta$ scheme.

First, recall that for the renormalized QMD, the BCS ratio $T_c/\bar{\Delta}_{\mathrm{gap},0} = e^{\gamma}/\pi$ is recovered both in the limit $\mu \to \infty$ and $\bar{\Delta}_{\mathrm{gap},0} \to 0$, see Eqs. (74) and (75). The solid gray curve in the left panel of Fig. 6 shows the analytic result for $T_c/\bar{\Delta}_{\mathrm{gap},0}$ obtained from the closed-form analytic expressions in Eqs. (72) and (D11) for the renormalized model, whereas the dashed line indicates the BCS ratio $T_c/\bar{\Delta}_{\mathrm{gap},0} = e^{\gamma}/\pi$. Accordingly, the analytic curve approaches the dashed BCS line smoothly at both ends: once as $\bar{\Delta}_{\mathrm{gap},0} \to 0$ and once as $\mu \to \infty$, the latter using the asymptotic gap $\bar{\Delta}_{\mathrm{gap},0}$ from Eq. (61). The lower endpoint $\bar{\Delta}_{\mathrm{gap},0} \to 0$ is, however, never realized in the physical calculation with finite quark masses (colored curves): In all approximations, the 2SC phase is reached through a first-order transition at a finite gap (see Fig. 2), so only the high-density limit $\mu \to \infty$ is able to approach the BCS ratio in practice. At large chemical potential, the quark mass vanishes, and all three curves satisfy the BCS relation Eq. (75). The calculation with physical quark masses in the renormalized model (red curve) lies almost exactly on top of the analytic curve obtained for massless quarks, demonstrating that explicit chiral-symmetry breaking has only a minor effect. Finally, the regularized model (blue curve) never shows the BCS scaling. Its multivalued behavior is a cutoff artifact: at large μ the finite three–momentum cutoff forces $\bar{\Delta}_{\mathrm{gap}}$ to decrease (see Fig. 2), which causes the curve to bend back on itself. Even within the displayed range, the slope of $T_c/\bar{\Delta}_{\mathrm{gap},0}$ differs substantially from the BCS value, and no systematic BCS behavior is visible. The values in the lower-left corner correspond to the point in the phase diagram where both the diquark condensate and the 2SC phase boundary drop to zero, at $\mu \simeq 686.5$ MeV (see Figs. 1 and 2).

In the right panel of Fig. 6, the solid gray curve depicts the analytic result for the $\sigma\Delta$ scheme for $\sigma = 0$. In this

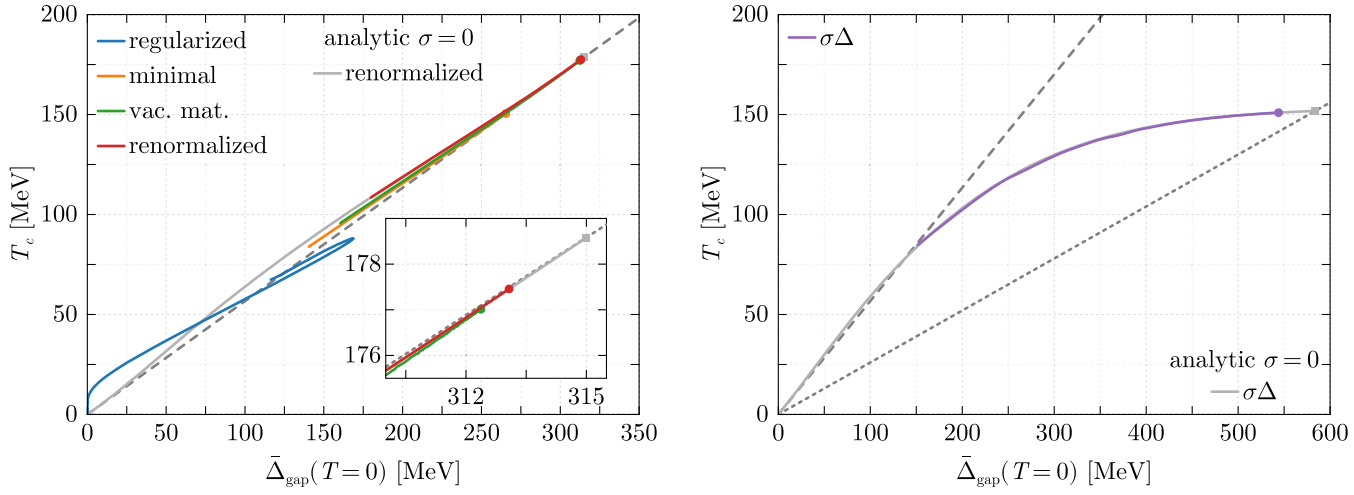

FIG. 6. Critical temperature T_c against the diquark gap at vanishing temperature $\bar{\Delta}_{\mathrm{gap}}(T=0)$. The gray solid lines indicate results obtained analytically for $\sigma = 0$, see Eqs. (72) and (D11), and solid squares mark their limits at $\mu \to \infty$. Solid dots are obtained numerically at $\mu = 4$ GeV. The dashed gray lines indicate the BCS scaling relation $T_c = 0.567\bar{\Delta}_{\mathrm{gap}}(T=0)$, while the dotted gray line indicates the asymptotic ratio of the $\sigma\Delta$ scheme obtained for our parameter choice, $T_c = 0.260\bar{\Delta}_{\mathrm{gap}}(T=0)$.

scheme, the BCS ratio (dashed gray line) is reached only in the $\bar{\Delta}_{\mathrm{gap},0} \to 0$ limit, which explains why the curve touches the dashed BCS line in the lower-left corner. At the opposite end, $\mu \to \infty$, the scaling deviates from the BCS value toward the computed value of $T_c/\bar{\Delta}_{\mathrm{gap},0} = 0.260$, shown in the gray dotted curve. So the analytic curve bends away from the dashed line and toward the dotted line at the end, as expected. As in the other schemes, the lower-left corner is never realized once the chiral dynamics is included. The purple curve in the right panel of Fig. 6, which incorporates finite quark masses in the $\sigma\Delta$ scheme, follows the analytic chiral-limit curve almost perfectly but starts at a nonzero lower value of the gap. This starting point is almost exactly on the BCS line, but we consider this to be accidental.

As discussed in Sec. V D, the $\sigma\Delta$ scheme yields a different asymptotic value for the diquark gap, yet, the critical temperature approaches the same limit as in the minimal scheme, consistent with Eq. (76). This similarity and distinction is clearly visible in comparing the two panels of Fig. 6. Therefore among the RGC schemes discussed in this paper, only the $\sigma\Delta$ scheme fails to follow the BCS relation at $\mu \to \infty$. Finally, we note that in the $\sigma\Delta$ scheme the asymptotic regime is reached only at much larger chemical potentials than in the other schemes. Near the asymptotic point (gray square), T_c remains almost constant while $\bar{\Delta}_{\mathrm{gap}}$ continues to grow, so no extended linear window develops around the dotted line in the right panel of Fig. 6. Even at $\mu = 4$ GeV (solid purple dot) the system is still far from its asymptotic point (gray square).

We conclude that although both the $\sigma\Delta$ and the vacuum matching schemes employ the same set of vacuum parameters, the additional field dependent subtractions in the $\sigma\Delta$ scheme leads to a distinct behavior of the diquark gap and entropy density (cf. Figs. 2 and 5). As noted in Ref. [17], such subtractions in RGC schemes can yield unexpected consequences, not anticipated from a physical standpoint, for example regarding the melting pattern of the different diquark condensates. The discrepancy observed here regarding the BCS relation is of the same nature; the additional subtraction in all Δ-dependent RGC schemes (including schemes used in Ref. [10] and mass-dependent and massless schemes in Ref. [17]) results in a deviation from the expected BCS relation.[8] It should be stressed that we employ the BCS relation only as a convenient diagnostic. It is derived for conventional (phonon-mediated) superconductors and therefore should *not* be viewed as a rigorous benchmark for color-superconducting models, where the pairing mechanism and underlying dynamics are qualitatively different and no experimental confirmation of the ratio exists.

It is also worth noting that the extent to which the BCS relation is realized and how the asymptotic limit is approached are sensitive to the choice of parameters. With different parameter choices, the BCS relation might become a good approximation only at substantially larger values of μ. Thus, the linear scaling along a large range of $\bar{\Delta}_{\mathrm{gap}}$ values observed in Figs. 6 and 6 (left) may be coincidental.

VII. SUMMARY, DISCUSSION AND CONCLUSIONS

In this work, we have presented a systematic comparison between two conceptually distinct approaches for rendering the two-flavor quark-meson-diquark (QMD) model ultraviolet complete: a *renormalized* formulation, and an *RG-consistent* mean-field treatment that incorporates ideas from the functional renormalization group. In order to make the comparison meaningful, we fix the couplings in both approaches to a common set of vacuum parameters, related to low-energy properties of the model. With this vacuum fit, they yield descriptions of cold and dense quark matter that are not only qualitatively but also, to a large extent, quantitatively consistent. Both frameworks generate similar qualitative phase structures, approach the Stefan-Boltzmann limit at large chemical potential, respect the BCS relation $T_c = e^{\gamma}\bar{\Delta}_{\mathrm{gap},0}/\pi$ (with the exception of the $\sigma\Delta$ scheme) and avoid the cutoff artifacts that typically affect naïvely regularized mean-field calculations.

Our analysis reveals that the regularized mean-field approximation with explicit diquark degrees of freedom leads to *unphysical* thermodynamics at high densities and temperatures. In particular, the pressure grows only linearly with μ, the Stefan-Boltzmann limit is never reached, and the speed of sound diverges, signaling a breakdown of the approximation.

Both renormalization and RG consistent treatment cure these artifacts. The two approaches nevertheless differ in important details. In the renormalized model, all vacuum and medium divergences are absorbed into scale-dependent bare couplings, rendering the effective action completely independent of the regulator. The price for this regulator independence is an enlarged parameter space: additional couplings proportional to $\phi^2|\Delta|^2$, $|\Delta|^4$ and, via the diquark wave function renormalization, to $\mu^2|\Delta|^2$ must be allowed to run with the cutoff. In contrast, RG-consistent mean-field schemes retain a fixed microscopic action and compensate for the residual cutoff dependence by imposing renormalization group consistency through suitable matching conditions.

Although an RG-consistent (RGC) mean-field construction ensures that physical observables become independent of the ultraviolet cutoff in the limit $\Lambda \to \infty$, it does not uniquely determine how to eliminate medium-induced

[8]We note that those subtractions are motivated by considerations *beyond* MFA. At the mean-field level they are not required, but once bosonic fluctuations are taken into account they may become essential.

divergences. The corresponding counterterms are therefore scheme-dependent, and different prescriptions can affect finite-density observables even after the vacuum parameters have been fixed. In Ref. [17], it was shown how these schemes can be related to the wave function renormalization of the diquark field, Z_Δ. Motivated by this insight, we introduce a vacuum-matching RGC scheme in which Z_Δ is fixed in the vacuum, facilitating direct comparisons with other approaches.

With this choice, the in-medium flow reproduces the diquark gap obtained in the fully renormalized QMD model up to subleading $1/\mu^2$ corrections, while preserving the cutoff independence characteristic of all RGC constructions. In this sense, the vacuum-matching scheme retains the conceptual clarity of the prescription in Ref. [10] as well as the minimal prescription in Ref. [17].

A final crisp benchmark is the BCS relation, $T_c = e^\gamma \bar{\Delta}_{\mathrm{gap}}(T=0)/\pi$. We find that this ratio is *exactly* reproduced in the $\mu \to \infty$ limit by the renormalized QMD model and by RG-consistent schemes whose medium subtraction can be reinterpreted as a diquark wave function renormalization, specifically, the minimal and vacuum-matching variants. In contrast, schemes in which the subtraction acquires an additional Δ-dependent structure (such as the $\sigma\Delta$ scheme of Ref. [10]) violate the BCS ratio. This underscores, once again, that seemingly innocuous choices for removing medium divergences can significantly alter key in-medium observables.

We emphasize, however, that this should *not* be taken as a criterion for discarding specific RG-consistent schemes, since it is unclear whether the BCS relation is actually realized within the regime of applicability of such models. Rather, this observation highlights the intrinsic scheme dependence associated with the subtraction of medium divergences, an ambiguity that persists even after matching to vacuum parameters. If one assumes that the BCS relation is indeed realized (or, alternatively, that the renormalized MFA represents the most reliable description), our results could be used to disfavor the $\sigma\Delta$ scheme. However, the present analysis is based solely on the MFA, and the $\sigma\Delta$ scheme may become mandatory once fluctuations beyond mean field are taken into account, see Ref. [10]. Consequently, more detailed analyses are required to clarify the origin and implications of this scheme dependency.

Our analytic solution of the $T = 0$ gap equation reveals that, in the limit $\mu \to \infty$, the diquark gap approaches a *finite* constant—see Eqs. (61) and (62). Remarkably, in both the renormalized model and RGC vacuum-matching scheme, this asymptotic value depends *only* on the vacuum quark mass, the diquark Yukawa coupling, and the vacuum wave function renormalization of the diquark field, with every explicit trace of the UV regulator eliminated. Renormalization and RG consistency thus remove the cutoff from the formalism without severing the link between vacuum physics and dense-matter observables: once the vacuum parameters are fixed, the entire finite-T / finite-μ sector of the QMD model becomes a genuine prediction of mean-field dynamics.

The most compelling next step is therefore to determine off-shell correlators directly from QCD—for example, via lattice calculations or by matching to continuum FRG/DSE computations. Such an *ab-initio* calibration would render the model a parameter-free tool for exploring the phase structure and equation of state of dense matter. This procedure would provide a decisive test of whether a mean-field QMD model, once anchored to realistic vacuum observables, can simultaneously satisfy astrophysical constraints without the need to incorporate beyond-mean-field fluctuations.

With the vacuum parameter fixing provided by first-principles QCD in place, several phenomenologically important extensions become both natural and reliable. For instance, the present two-flavor framework can be generalized to the three-flavor case. In Ref. [17], the melting pattern of the color–flavor-locked (CFL) phase was analyzed within an RG-consistent NJL framework, successfully reproducing earlier Ginzburg-Landau predictions [20], in contrast to the failure of conventional cutoff-regularized NJL models. It would be instructive to extend this analysis to a three-flavor QMD model.

For astrophysical applications, a repulsive vector interaction, together with electric charge, isospin and color-neutrality constraints, must be incorporated to obtain an equation of state compatible with $\sim 2M_\odot$ neutron stars and their tidal-deformability bounds [64,66–69]. In addition, the regulator-independent framework developed here provides a clean setting to revisit spatially modulated chiral or pairing phases, whose very existence crucially depends on careful control of cutoff artifacts [70–72]. Work along these lines is ongoing and will be reported elsewhere.

Since many earlier hybrid-star studies rely on regMFA diquark equations of state at high densities, they inevitably inherit unphysical artifacts, potentially leading to erroneous conclusions regarding stellar properties. A properly renormalized or RG-consistent treatment is therefore essential to ensure reliable astrophysical predictions. In this work, we have demonstrated that both renormalization and RG consistency eliminate the regulator ambiguities in the QMD model, yielding mutually consistent and analytically tractable descriptions of dense quark matter. Together, these approaches provide a powerful and flexible framework for future studies aiming to bridge microscopic QCD dynamics with astrophysical observations of compact stars.

ACKNOWLEDGMENTS

We thank Marco Hofmann and Shreedhar Rajesh for collaboration on related topics, and Jan M. Pawlowski and Lorenz von Smekal for valuable discussions. H. G. further acknowledges insightful conversations with Jens Andersen, Jens Braun, Tomáš Brauner, Andreas Geissel, Mathias

Nødtvedt, and Dirk Rischke, and U. M. thanks Janos Polonyi for discussions. The authors gratefully acknowledge support from the Helmholtz Graduate School for Hadron and Ion Research (HGS-HIRe) for FAIR, the GSI Helmholtzzentrum für Schwerionenforschung, and the Deutsche Forschungsgemeinschaft (DFG, German Research Foundation) through the CRC-TR211 "Strong-interaction matter under extreme conditions" Project No. 315477589–TRR 211.

DATA AVAILABILITY

The data that support the findings of this article are openly available [73], embargo periods may apply.

APPENDIX A: DERIVATION OF THE RENORMALIZED POTENTIAL

Fixing $\tilde{f}_\pi$, the remaining vacuum parameters in Table I are found by evaluating derivatives of the effective potential Eq. (3) in vacuum, which yields

$$\tilde{m}_\sigma^2 = m_\phi^2(\Lambda) + 3\lambda_\phi(\Lambda)\tilde{f}_\pi^2 + (\partial_\sigma^2 L_\Lambda)|_{\text{vac}}, \tag{A1}$$

$$\tilde{m}_\Delta^2 = m_\Delta^2(\Lambda) + \frac{1}{2}\lambda_{\text{mix}}(\Lambda)\tilde{f}_\pi^2 + \frac{1}{2}(\partial_\Delta^2 L_\Lambda)|_{\text{vac}}, \tag{A2}$$

$$\tilde{\lambda}_{\text{mix}} = \lambda_{\text{mix}}(\Lambda) + \frac{1}{2}(\partial_\sigma^2\partial_\Delta^2 L_\Lambda)|_{\text{vac}}, \tag{A3}$$

$$\tilde{\lambda}_\Delta = \lambda_\Delta(\Lambda) + \frac{1}{24}(\partial_\Delta^4 L_\Lambda)|_{\text{vac}}, \tag{A4}$$

$$\tilde{Z}_\Delta = Z_\Delta(\Lambda) - \frac{1}{16}(\partial_\mu^2\partial_\Delta^2 L_\Lambda)|_{\text{vac}}. \tag{A5}$$

Eq. (20) and Eqs. (A1) to (A5) form a simple linear system of equations that can be solved for an expression of the 6 UV scale-dependent bare parameters in terms of the correlators. The solution of this linear system yields

$$m_\phi^2(\Lambda) = -\frac{1}{2\tilde{f}_\pi}\{\tilde{m}_\sigma^2\tilde{f}_\pi - 3c - \tilde{f}_\pi(\partial_\sigma^2 L_\Lambda)|_{\text{vac}} + 3(\partial_\sigma L_\Lambda)|_{\text{vac}}\}, \tag{A6}$$

$$m_\Delta^2(\Lambda) = \tilde{m}_\Delta^2 - \frac{1}{2}\tilde{\lambda}_{\text{mix}}\tilde{f}_\pi^2 - \frac{1}{2}(\partial_\Delta^2 L_\Lambda)\Big|_{\text{vac}} + \frac{\tilde{f}_\pi^2}{4}(\partial_\sigma^2\partial_\Delta^2 L_\Lambda)\Big|_{\text{vac}}, \tag{A7}$$

$$\lambda_\phi(\Lambda) = \frac{1}{2\tilde{f}_\pi{}^3}\{\tilde{m}_\sigma^2\tilde{f}_\pi - c - \tilde{f}_\pi(\partial_\sigma^2 L_\Lambda)|_{\text{vac}} + (\partial_\sigma L_\Lambda)|_{\text{vac}}\}, \tag{A8}$$

$$\lambda_{\text{mix}}(\Lambda) = \tilde{\lambda}_{\text{mix}} - \frac{1}{2}(\partial_\sigma^2\partial_\Delta^2 L_\Lambda)\Big|_{\text{vac}}, \tag{A9}$$

$$\lambda_\Delta(\Lambda) = \tilde{\lambda}_\Delta - \frac{1}{24}(\partial_\Delta^4 L_\Lambda)\Big|_{\text{vac}}, \tag{A10}$$

$$Z_\Delta(\Lambda) = \tilde{Z}_\Delta + \frac{1}{16}(\partial_\mu^2\partial_\Delta^2 L_\Lambda)\Big|_{\text{vac}}. \tag{A11}$$

Using the expression for the loop contribution Eq. (4), we can write the bare parameters as

$$m_\phi^2(\Lambda) = -\frac{1}{2}\tilde{m}_\sigma^2 + \frac{3c}{2\tilde{f}_\pi} + 2N_f\int_{|\vec{p}|<\Lambda}\frac{3g_\phi^2}{2\epsilon_{q,\text{vac}}^3}(2p^2 + 3m_{q,\text{vac}}^2), \tag{A12}$$

$$m_\Delta^2(\Lambda) = \tilde{m}_\Delta^2 - \frac{1}{2}\tilde{\lambda}_{\text{mix}}\tilde{f}_\pi^2 + 2N_f\int_{|\vec{p}|<\Lambda}\frac{g_\Delta^2 p^2}{2\epsilon_{q,\text{vac}}^5}(2p^2 + 5m_{q,\text{vac}}^2), \tag{A13}$$

$$\lambda_\phi(\Lambda) = \frac{1}{2\tilde{f}_\pi^2}\tilde{m}_\sigma^2 - \frac{c}{2\tilde{f}_\pi^3} - 2N_f\int_{|\vec{p}|<\Lambda}\frac{3g_\phi^4}{2\epsilon_{q,\text{vac}}^3}, \tag{A14}$$

$$\lambda_{\text{mix}}(\Lambda) = \tilde{\lambda}_{\text{mix}} - 2N_f\int_{|\vec{p}|<\Lambda}\frac{g_\Delta^2 g_\phi^2}{\epsilon_{q,\text{vac}}^5}(p^2 - 2m_{q,\text{vac}}^2), \tag{A15}$$

$$\lambda_\Delta(\Lambda) = \tilde{\lambda}_\Delta - 2N_f\int_{|\vec{p}|<\Lambda}\frac{g_\Delta^4}{4\epsilon_{q,\text{vac}}^3}, \tag{A16}$$

$$Z_\Delta(\Lambda) = \tilde{Z}_\Delta - 2N_f\int_{|\vec{p}|<\Lambda}\frac{g_\Delta^2}{4\epsilon_{q,\text{vac}}^3}. \tag{A17}$$

Finally, we obtain the renormalized and UV scale independent potential by sending $\Lambda \to \infty$ in the momentum integration of the effective potential, which results in Eq. (21).

APPENDIX B: β-FUNCTIONS OF THE MODEL COUPLINGS

From the mean-field flow Eq. (34), we can evaluate the β-functions of the relevant couplings of the model. At vanishing temperature and for the sharp regulator, the mean-field flow reduces to

$$\partial_k\Omega_k = \frac{N_f k^2}{\pi^2}\{\epsilon_q(k) + E_q^-(k) + E_q^+(k) - \epsilon_q^-(k)\theta(\epsilon_q^-(k))\}. \tag{B1}$$

In the following, we neglect the last term $-\epsilon_q^-(k)\theta(\epsilon_q^-(k))$ arising from the thermal part of the potential, as it yields an irrelevant contribution in the limit $k \to \infty$. We then perform a Taylor expansion of the effective potential

$$\Omega_k = \frac{1}{2}m_{\phi,k}^2\phi^2 + \frac{1}{4}\lambda_{\phi,k}\sigma^4 + \frac{1}{2}\lambda_{\mathrm{mix},k}\sigma^2\Delta^2 + m_{\Delta,k}^2\Delta^2 + \lambda_{\Delta,k}\Delta^4 - 4Z_{\Delta,k}\mu^2\Delta^2 + \cdots, \tag{B2}$$

and insert this expansion in the mean-field flow Eq. (B1). The β-functions of the couplings are obtained by comparing coefficients, yielding

$$\partial_k m_{\phi,k}^2 = \frac{6g_\phi^2}{\pi^2}k, \quad \partial_k\lambda_{\phi,k} = -\frac{3g_\phi^4}{\pi^2}\frac{1}{k}, \quad \partial_k m_{\Delta,k}^2 = \frac{2g_\Delta^2}{\pi^2}k,$$
$$\partial_k\lambda_{\Delta,k} = -\frac{g_\Delta^4}{2\pi^2}\frac{1}{k}, \quad \partial_k\lambda_{\mathrm{mix},k} = -\frac{2g_\Delta^2 g_\phi^2}{\pi^2}\frac{1}{k}, \quad \partial_k Z_{\Delta,k} = -\frac{g_\Delta^2}{2\pi^2}\frac{1}{k}. \tag{B3}$$

This directly leads to the following solutions for the scale dependence of the couplings:

$$m_{\phi,k}^2 = \frac{3g_\phi^2}{\pi^2}(k^2 - {k_0}^2) + m_{\phi,k_0}^2, \tag{B4}$$

$$\lambda_{\phi,k} = -\frac{3g_\phi^4}{\pi^2}\ln\frac{k}{k_0} + \lambda_{\phi,k_0}, \tag{B5}$$

$$m_{\Delta,k}^2 = \frac{g_\Delta^2}{\pi^2}(k^2 - {k_0}^2) + m_{\Delta,k_0}^2, \tag{B6}$$

$$\lambda_{\Delta,k} = -\frac{g_\Delta^4}{2\pi^2}\ln\frac{k}{k_0} + \lambda_{\Delta,k_0}, \tag{B7}$$

$$\lambda_{\mathrm{mix},k} = -\frac{2g_\Delta^2 g_\phi^2}{\pi^2}\ln\frac{k}{k_0} + \lambda_{\mathrm{mix},k_0}, \tag{B8}$$

$$Z_{\Delta,k} = -\frac{g_\Delta^2}{2\pi^2}\ln\frac{k}{k_0} + Z_{\Delta,k_0}. \tag{B9}$$

Here, k_0 represents an arbitrary reference scale. Notably, if we choose $k = \Lambda$, the RG scale dependence of the couplings exactly matches the Λ-dependence of the renormalized model couplings, as given in Eqs. (11) to (16). This explicitly demonstrates that, as expected, the RG-consistency generates the appropriate counterterms introduced in the renormalized model.

APPENDIX C: BCS ANALYSIS AT T_c

Subtraction of the gap equations in Eq. (69) yields the relation

$$\left.\frac{\partial\Omega_{\mathrm{ren}}^{\mathrm{eff}}(\sigma,\Delta;0,\mu)}{\partial\Delta^2}\right|_{\substack{\sigma=0\\ \Delta=\bar{\Delta}_0}} - \left.\frac{\partial\Omega_{\mathrm{ren}}^{\mathrm{eff}}(\sigma,\Delta;T_c,\mu)}{\partial\Delta^2}\right|_{\substack{\sigma=0\\ \Delta=0}} = 2\tilde{\lambda}_\Delta\bar{\Delta}_0^2 - N_f g_\Delta^2\int_{\vec{p}}\left\{\frac{1}{E_{q,0}^-} + \frac{1}{E_{q,0}^+} + \frac{\bar{\Delta}_{\mathrm{gap},0}^2}{\epsilon_{q,\mathrm{vac}}^3} - \frac{1}{\epsilon_q^-}\tanh\frac{\epsilon_q^-}{2T_c} - \frac{1}{\epsilon_q^+}\tanh\frac{\epsilon_q^+}{2T_c}\right\}, \tag{C1}$$

where, assuming a vanishing chiral condensate, we have

$$E_{q,0}^\pm = \sqrt{(\epsilon_q^\pm)^2 + \bar{\Delta}_{\mathrm{gap},0}^2}, \qquad \epsilon_q^\pm = p \pm \mu,$$

with $p = |\vec{p}|$. Since both gap equations vanish, their difference also vanishes. The resulting condition implicitly defines the location of the second-order phase boundary of the 2SC phase at a given chemical potential μ, which is determined by the corresponding zero-temperature gap $\bar{\Delta}_0(\mu) \equiv \bar{\Delta}(T = 0, \mu)$. Solving this condition for T yields the critical temperature T_c.

To proceed, we split the remaining momentum integral into two convergent parts, one for each tanh term. Because each part converges separately, we can shift and unify the integration limits. Rewriting Eq. (C1) in this way, we obtain

$$0 = 2\tilde{\lambda}_\Delta\bar{\Delta}_0^2 - g_\Delta^2 N_f\left\{\int_{\vec{p}}\left(\frac{1}{2}\frac{\bar{\Delta}_{\mathrm{gap},0}^2}{\epsilon_{q,\mathrm{vac}}^3} + \frac{1}{E_{q,0}^-} - \frac{1}{\epsilon_q^-}\tanh\frac{\epsilon_q^-}{2T_c}\right) + \int_{\vec{p}}\left(\frac{1}{2}\frac{\bar{\Delta}_{\mathrm{gap},0}^2}{\epsilon_{q,\mathrm{vac}}^3} + \frac{1}{E_{q,0}^+} - \frac{1}{\epsilon_q^+}\tanh\frac{\epsilon_q^+}{2T_c}\right)\right\}. \tag{C2}$$

By shifting the integration variable in the first integral, $p \to p - \mu$, and in the second integral, $p \to p + \mu$, and then separating the even and odd parts of the integrand, the two integrals can be combined into a single one,

$$0 = 2\tilde{\lambda}_\Delta\bar{\Delta}_0^2 - g_\Delta^2 N_f\int_{\vec{p}}\frac{1}{p^2}\left\{\frac{\bar{\Delta}_{\mathrm{gap},0}^2(p-\mu)^2}{2((p-\mu)^2 + m_{q,\mathrm{vac}}^2)^{3/2}} + \frac{\bar{\Delta}_{\mathrm{gap},0}^2(p+\mu)^2}{2((p+\mu)^2 + m_{q,\mathrm{vac}}^2)^{3/2}} + \frac{(p-\mu)^2}{\sqrt{p^2 + \bar{\Delta}_{\mathrm{gap},0}^2}} + \frac{(p+\mu)^2}{\sqrt{p^2 + \bar{\Delta}_{\mathrm{gap},0}^2}} - 2(p^2+\mu^2)\frac{1}{p}\tanh\left(\frac{p}{2T_c}\right)\right\}. \tag{C3}$$

The integral can be evaluated analytically by inserting the series representation

$$\tanh(x) = 2\sinh(x)\sum_{k=1}^{\infty}(-1)^{k+1}e^{(1-2k)x} = 2e^{-x}\sinh(x) + 2\sinh(x)\sum_{k=2}^{\infty}(-1)^{k+1}e^{(1-2k)x}. \tag{C4}$$

For all $k \geq 2$, the resulting terms can be integrated using

$$\int_0^\infty dx(x^2+\alpha^2)\frac{1}{x}\sinh(x)\sum_{k=2}^{\infty}(-1)^{k+1}e^{(1-2k)x} = \sum_{k=2}^{\infty}(-1)^k\left(\frac{2k-1}{4(k-1)^2k^2}+\alpha^2\ln\left(\frac{k}{k-1}\right)\right), \quad \text{(C5)}$$

with $\alpha\in\mathbb{R}$. The first part is summed to

$$\sum_{k=2}^{\infty}(-1)^k\frac{2k-1}{(k-1)^2k^2}=\frac{\pi^2}{6}-1 \quad \text{(C6)}$$

and the second part can be simplified using

$$\begin{aligned}\sum_{k=2}^{\infty}(-1)^k\ln\left(\frac{k}{k-1}\right) &= \sum_{m=1}^{\infty}(-1)^{2m}\ln\left(\frac{2m}{2m-1}\right) - (-1)^{2m+1}\ln\left(\frac{2m+1}{2m}\right)\\ &= -\ln\left(\prod_{k=1}^{\infty}\left(1-\frac{1}{4k^2}\right)\right), \end{aligned} \quad \text{(C7)}$$

with the infinite product value of $\prod_{k=1}^{\infty}(1-\frac{1}{4k^2})=\frac{2}{\pi}$. This contributions to Eq. (C5) is

$$\alpha^2\sum_{k=2}^{\infty}2(-1)^k\ln\left(\frac{k}{k-1}\right)=\alpha^2(-\ln 2+\ln\pi). \quad \text{(C8)}$$

The remaining contribution from the $k=1$ term in Eq. (C4), together with the remaining terms of Eq. (C3) is obtained by use of an integral of the form

$$\int_0^\infty dx\left\{-\frac{1}{1+x}+\frac{2}{x}e^{-x}\sinh(x)\right\}=\ln 2+\gamma, \quad \text{(C9)}$$

where $\gamma\simeq 0.5772$ is the Euler-Mascheroni constant. Summing all contributions for the integral in Eq. (C3), this whole expression can be evaluated as

$$0=2\tilde{\lambda}_\Delta\bar{\Delta}_0^2-\frac{g_\Delta^2}{6\pi^2}\left\{2\pi^2T_c^2+12\mu^2\left(\ln\frac{\pi T_c}{\bar{\Delta}_{\mathrm{gap},0}}-\gamma\right)+3\Delta_{\mathrm{gap},0}^2\left(2\ln\frac{\bar{\Delta}_{\mathrm{gap},0}}{m_{q,\mathrm{vac}}}-1\right)\right\}. \quad \text{(C10)}$$

The expression above can be rewritten as

$$\left(\frac{\pi^2}{3\mu^2}T_c^2\right)\exp\left(\frac{\pi^2}{3\mu^2}T_c^2\right)=\frac{\bar{\Delta}_{\mathrm{gap},0}^2}{3\mu^2}\exp\left[2\gamma+\frac{\bar{\Delta}_{\mathrm{gap},0}^2}{\mu^2}\left(\frac{1}{2}+\frac{2\pi^2}{g_\Delta^4}\tilde{\lambda}_\Delta-\ln\frac{\bar{\Delta}_{\mathrm{gap},0}}{m_{q,\mathrm{vac}}}\right)\right]. \quad \text{(C11)}$$

Now, starting from the transcendental equation

$$ze^z=C, \quad \text{(C12)}$$

one introduces the (multivalued) *Lambert W-function* [74], defined implicitly by

$$W(x)e^{W(x)}=x. \quad \text{(C13)}$$

Applying this definition to Eq. (C12) gives the formal solution[9]

$$z=W(C). \quad \text{(C14)}$$

Employing Eq. (C14), the critical temperature T_c in Eq. (C11) can be written compactly as

$$T_c^2(\bar{\Delta}_0,\mu)=\frac{3\mu^2}{\pi^2}W\left(\frac{\bar{\Delta}_{\mathrm{gap},0}^2}{3\mu^2}\exp\left[2\gamma+\frac{\bar{\Delta}_{\mathrm{gap},0}^2}{\mu^2}\left(\frac{1}{2}+\frac{2\pi^2}{g_\Delta^4}\tilde{\lambda}_\Delta-\ln\frac{\bar{\Delta}_{\mathrm{gap},0}}{m_{q,\mathrm{vac}}}\right)\right]\right), \quad \text{(C15)}$$

where the branch of the W-function must be chosen such that the second root is positive and the resulting T_c is real and positive. Furthermore, T_c can also be expressed purely in terms of the chemical potential μ. To derive this relation, we start from the gap equation Eq. (58) and establish the following identity

$$\ln\frac{\bar{\Delta}_{\mathrm{gap},0}}{m_{q,\mathrm{vac}}}=\frac{\tilde{m}_\Delta^2+2\tilde{\lambda}_\Delta\bar{\Delta}_0^2-4\tilde{Z}_\Delta\mu^2-\frac{1}{2}\tilde{\lambda}_{\mathrm{mix}}\tilde{f}_\pi^2+\frac{g_\Delta^2}{2\pi^2}(\bar{\Delta}_{\mathrm{gap},0}^2+2\mu^2-3m_{q,\mathrm{vac}}^2)}{\frac{g_\Delta^2}{\pi^2}(\bar{\Delta}_{\mathrm{gap},0}^2-2\mu^2)}. \quad \text{(C16)}$$

Plugging the above identity into Eq. (C15), all Δ-dependence cancels out, and we obtain an explicit expression for T_c that depends *only* on the chemical potential μ

[9]For real arguments $C\in[-e^{-1},\infty)$ the Lambert W function has exactly two real branches: the principal branch $W_0(C)\geq -1$ and the secondary branch $W_{-1}(C)\leq -1$. Consequently, Eq. (C14) can supply up to two distinct real roots, one from each branch. For $C<-e^{-1}$ the two real branches combine and become complex. Detailed discussions of these branches may be found in Refs. [74,75].

$$T_c^2(\mu) = \frac{3\mu^2}{\pi^2} W\left(\frac{m_{q,\mathrm{vac}}^2}{3\mu^2}\exp\left[-1+2\gamma+\frac{4\pi^2\tilde{Z}_\Delta}{g_\Delta^2}+\frac{1}{2\mu^2}\left(3m_{q,\mathrm{vac}}^2+\frac{\pi^2}{g_\Delta^2}(\tilde{\lambda}_{\mathrm{mix}}\tilde{f}_\pi^2-2\tilde{m}_\Delta^2)\right)\right]\right). \tag{C17}$$

Taking the limit $\mu \to \infty$ of the above equation yields

$$\lim_{\mu\to\infty} T_c(\mu) = \frac{e^\gamma}{\pi} m_{q,\mathrm{vac}} \exp\left(-\frac{1}{2}+\frac{2\pi^2\tilde{Z}_\Delta}{g_\Delta^2}\right) = \frac{e^\gamma}{\pi}\lim_{\mu\to\infty}\bar{\Delta}_{\mathrm{gap},0}, \tag{C18}$$

which is the BCS relation Eq. (51). Additionally, taking the weak-coupling limit $\bar{\Delta}_{\mathrm{gap},0} \to 0$ of $T_c/\bar{\Delta}_{\mathrm{gap},0}$, from Eq. (C15) we find

$$\lim_{\bar{\Delta}_{\mathrm{gap},0}\to 0}\frac{T_c}{\bar{\Delta}_{\mathrm{gap},0}} = \frac{e^\gamma}{\pi}, \tag{C19}$$

which agrees with the standard BCS ratio. This explains why the analytic curve in Fig. 6 approaches the BCS line at both ends: once for $\mu \to \infty$ and once for $\bar{\Delta}_{\mathrm{gap},0} \to 0$.

APPENDIX D: ANALYTIC RGC SCHEMES EXPRESSION AT $\sigma = 0$

In this Appendix, we provide the analysis for the case $\sigma = 0$, leading to expressions for the diquark gap at $T = 0$ and the dependence of the critical temperature on the chemical potential μ for all RGC schemes presented in this work. To obtain the expression for critical temperature, we follow the same procedure as in Appendix C.

1. Minimal scheme

Starting from the effective potential given in Eq. (42) and the minimal scheme ansatz in Eq. (44), and taking the limit $\Lambda \to \infty$, the gap equation for the diquark field becomes

$$\begin{aligned}\left.\frac{\partial\Omega_{\min}^{\mathrm{eff}}(\sigma,\Delta;0,\mu)}{\partial\Delta}\right|_{\substack{\sigma=0\\ \Delta=\bar{\Delta}_0}} &= 2\bar{\Delta}_0\left[m_\Delta^2 - 4Z_\Delta\mu^2 + \frac{g_\Delta^2}{\pi^2}\left(-\Lambda'\sqrt{\Lambda'^2+\bar{\Delta}_{\mathrm{gap},0}^2} + \bar{\Delta}_{\mathrm{gap},0}^2\,\mathrm{artanh}\frac{\Lambda'}{\sqrt{\Lambda'^2+\bar{\Delta}_{\mathrm{gap},0}^2}} + \mu^2\left(3+\ln\frac{\bar{\Delta}_{\mathrm{gap},0}^2}{4\Lambda'^2}\right)\right)\right] \\ &= 0.\end{aligned} \tag{D1}$$

Solving this equation for μ^2 and identifying for which value of the diquark gap does μ^2 diverge, similarly to Sec. V B, one finds the asymptotic diquark gap to be

$$\lim_{\mu\to\infty}\bar{\Delta}_{\mathrm{gap},0}^{(\min)} = 2\Lambda'\exp\left(-\frac{3}{2}+\frac{2\pi^2}{g_\Delta^2}Z_\Delta\right), \tag{D2}$$

as given by Eq. (62). Following the procedure outlined in Appendix C, we obtain the equation for T_c as

$$T_c^2(\bar{\Delta}_0,\mu) = \frac{3\mu^2}{\pi^2} W\left(\frac{\bar{\Delta}_{\mathrm{gap},0}^2}{3\mu^2}\exp\left[2\gamma-\frac{\Lambda'^2}{\mu^2}\left(-1+\sqrt{1+\bar{\Delta}_{\mathrm{gap},0}^2/\Lambda'^2}\right)\right]\left(\frac{-1+\sqrt{1+\bar{\Delta}_{\mathrm{gap},0}^2/\Lambda'^2}}{1+\sqrt{1+\bar{\Delta}_{\mathrm{gap},0}^2/\Lambda'^2}}\right)^{-\frac{\bar{\Delta}_{\mathrm{gap},0}^2}{2\mu^2}}\right). \tag{D3}$$

Furthermore, making use of the identity

$$\frac{-\Lambda'+\sqrt{\Lambda'^2+\bar{\Delta}_{\mathrm{gap},0}^2}}{\Lambda'+\sqrt{\Lambda'^2+\bar{\Delta}_{\mathrm{gap},0}^2}} = \left(\frac{2\Lambda'}{\bar{\Delta}_{\mathrm{gap},0}}\right)^{-4\mu^2/\bar{\Delta}_{\mathrm{gap},0}^2}\exp\left[\frac{1}{\bar{\Delta}_{\mathrm{gap},0}^2}\left(-2\Lambda'\sqrt{\Lambda'^2+\bar{\Delta}_{\mathrm{gap},0}^2}+6\mu^2+\frac{2\pi^2}{g_\Delta^2}(m_\Delta^2-4Z_\Delta\mu^2)\right)\right], \tag{D4}$$

which follows from the gap equation Eq. (D1), the critical temperature T_c can be expressed as an explicit function of μ as

$$T_c^2(\mu) = \frac{3\mu^2}{\pi^2} W\left(\frac{4\Lambda'^2}{3\mu^2}\exp\left[-3+2\gamma+\frac{\pi^2(4Z_\Delta - m_\Delta^2/\mu^2)}{g_\Delta^2}+\frac{\Lambda'^2}{\mu^2}\right]\right). \tag{D5}$$

Taking $\mu \to \infty$, we get

$$\lim_{\mu\to\infty} T_c(\mu) = \frac{2\Lambda'}{\pi}\exp\left(\gamma - \frac{3}{2} + \frac{2\pi^2}{g_\Delta^2} Z_\Delta\right) \tag{D6}$$

$$= \lim_{\mu\to\infty} \frac{e^\gamma}{\pi}\bar{\Delta}_{\mathrm{gap},0}, \tag{D7}$$

yielding the BCS relation.

2. Vacuum matching scheme

As the vacuum matching scheme is a variant of the minimal scheme with a special value for $\tilde{Z}_\Delta$, both schemes are similar. This is directly seen by computing the gap equation

$$\left.\frac{\partial\Omega^{\mathrm{eff}}_{\mathrm{vm}}(\sigma,\Delta;0,\mu)}{\partial\Delta}\right|_{\substack{\sigma=0\\ \Delta=\bar{\Delta}_0}} = 0, \tag{D8}$$

which yields the same expression as Eq. (D1) with the replacement $Z_\Delta \to Z'_\Delta$ where

$$Z'_\Delta = Z_\Delta - \frac{g_\Delta^2}{2\pi^2}\left(\ln\frac{2\Lambda'}{m_{q,\mathrm{vac}}} + \frac{\Lambda'}{\sqrt{\Lambda'^2 + m_{q,\mathrm{vac}}^2}} + 1 + \operatorname{artanh}\frac{\Lambda'}{\sqrt{\Lambda'^2 + m_{q,\mathrm{vac}}^2}}\right). \tag{D9}$$

All relations derived in the previous section can be recovered for the present scheme by the insertion of the above ansatz into Eq. (D2). In particular, the resulting asymptotic diquark gap coincides with Eq. (63), which in turn equals Eq. (61). Consequently, the BCS relation is obtained for this scheme as well.

3. $\sigma\Delta$ scheme

As discussed in the main text, the $\sigma\Delta$ scheme differs from the other two schemes because of its additional Δ- and σ-dependence. These extra Δ terms become particularly important, especially in deriving the BCS relation. Proceeding analogously to the previous cases, but starting from the ansatz Eq. (43) and taking the limit $\Lambda \to \infty$, we determine the asymptotic value of Δ by examining the pole of the gap equation in μ^2. This procedure yields

$$\begin{aligned} 0 = {} & 2g_\Delta^2\bar{\Delta}_{\mathrm{gap},0}^2\Lambda' - 4\pi^2 Z_\Delta \Lambda'^2\sqrt{\bar{\Delta}_{\mathrm{gap},0}^2 + \Lambda'^2} \\ & + g_\Delta^2(3\Lambda'^3 - 4\pi^2 Z_\Delta \bar{\Delta}_0^2\sqrt{\bar{\Delta}_{\mathrm{gap},0}^2 + \Lambda'^2}) \\ & - 2g_\Delta^2(\bar{\Delta}_{\mathrm{gap},0}^2 + \Lambda'^2)^{3/2}\operatorname{artanh}\frac{\Lambda'}{\sqrt{\bar{\Delta}_{\mathrm{gap},0}^2 + \Lambda'^2}}. \end{aligned} \tag{D10}$$

The equation above cannot be solved analytically for $\bar{\Delta}_{\mathrm{gap},0}$; in its current form only a numerical solution is feasible. Solving Eq. (D10) numerically with $Z_\Delta = 0$, $\Lambda' = 600$ MeV and $g_\Delta = 4.5$ gives the asymptotic diquark gap in the $\sigma\Delta$ scheme as $\lim_{\mu\to\infty}\bar{\Delta}_{\mathrm{gap}}^{(\sigma\Delta)} = 584.2$ MeV. Lastly, to obtain the critical temperature T_c we follow the procedure leading to Eq. (C1). This leads to the implicit equation

$$T_c^2(\bar{\Delta}_0,\mu) = \frac{3\mu^2}{\pi^2} W\left(\frac{4\Lambda'^2}{3\mu^2}\exp\left[-3 + 2\gamma - \frac{\Lambda'}{\mu^2}\left(-\Lambda' + \frac{(\bar{\Delta}_{\mathrm{gap},0}^2 + \Lambda'^2)^2 - (2\bar{\Delta}_{\mathrm{gap},0}^2 + 3\Lambda'^2)\mu^2}{(\bar{\Delta}_{\mathrm{gap},0}^2 + \Lambda'^2)^{3/2}}\right)\right]\left(\frac{-\Lambda' + \sqrt{\Lambda'^2 + \bar{\Delta}_{\mathrm{gap},0}^2}}{\Lambda' + \sqrt{\Lambda'^2 + \bar{\Delta}_{\mathrm{gap},0}^2}}\right)^{1 - \frac{\bar{\Delta}_{\mathrm{gap},0}^2}{2\mu^2}}\right). \tag{D11}$$

Using the following identity, derived from the gap equation

$$\begin{aligned} \frac{-\Lambda' + \sqrt{\Lambda'^2 + \bar{\Delta}_{\mathrm{gap},0}^2}}{\Lambda' + \sqrt{\Lambda'^2 + \bar{\Delta}_{\mathrm{gap},0}^2}} = \exp\Bigg[& -\frac{2}{g_\Delta^2(\bar{\Delta}_{\mathrm{gap},0}^2 + \Lambda'^2)^{3/2}(\bar{\Delta}_{\mathrm{gap},0}^2 - 2\mu^2)}\Big\{g_\Delta^2\Lambda'(\bar{\Delta}_{\mathrm{gap},0}^4 + 2\bar{\Delta}_{\mathrm{gap},0}^2(\Lambda'^2 - \mu^2) + \Lambda'^4 - 3\Lambda'^2\mu^2) \\ & - \pi^2\sqrt{\bar{\Delta}_{\mathrm{gap},0}^2 + \Lambda'^2}(\Lambda'^2 + g_\Delta^2\bar{\Delta}_{\mathrm{gap},0}^2)(m_\Delta^2 - 4Z_\Delta\mu^2)\Big\}\Bigg], \end{aligned} \tag{D12}$$

T_c can be expressed as an explicit function of μ as

$$T_c^2(\mu) = \frac{3\mu^2}{\pi^2} W\left(\frac{4\Lambda'^2}{3\mu^2}\exp\left[-3 + 2\gamma + \frac{\pi^2(4Z_\Delta - m_\Delta^2/\mu^2)}{g_\Delta^2} + \frac{\Lambda'^2}{\mu^2}\right]\right). \tag{D13}$$

Equation (D13) is the same as Eq. (D5), implying that the $\sigma\Delta$ scheme and the minimal scheme yield identical 2SC phase boundary for $\sigma = 0$. Taking $\mu \to \infty$ in Eq. (D13), we get

$$\lim_{\mu\to\infty} T_c(\mu) = \frac{2\Lambda'}{\pi}\exp\left(\gamma - \frac{3}{2} + \frac{2\pi^2}{g_\Delta^2}Z_\Delta\right), \tag{D14}$$

which is equal to Eq. (D6). However, within this scheme, the above equation does *not* reproduce the BCS relation. The reason is straightforward: if we insert the ansatz

$$\bar{\Delta}_{\mathrm{gap},0} = 2\Lambda'\exp\left(-\frac{3}{2} + \frac{2\pi^2}{g_\Delta^2}Z_\Delta\right),$$

into the gap equation and then take the limit $\mu \to \infty$, the right-hand side does *not* vanish. Consequently, this ansatz is *not* a solution of the gap equation in the $\sigma\Delta$ scheme, and the BCS relation does not hold in general.

APPENDIX E: BEHAVIOR OF REGMFA AT HIGH CHEMICAL POTENTIAL

In the regularized QMD model, as seen in Fig. 2, the diquark condensate vanishes at sufficiently large chemical potentials, leaving only a finite constituent quark mass which remains at a constant value. This behavior can be understood analytically as follows. For chemical potentials satisfying $\mu > \sqrt{\Lambda^2 + m_q^2}$, the loop contribution to the effective potential Eq. (4) at $T = 0$ reads

$$L_\Lambda(m_q, \Delta_{\mathrm{gap}}; T = 0) = -2N_f \int_{|\vec{p}|<\Lambda} \left\{ E_q^+ + E_q^- + \frac{1}{2}\epsilon_q^+ + \frac{1}{2}|\epsilon_q^-| \right\}. \tag{E1}$$

Expanding this expression in powers of Δ/Λ gives

$$L_\Lambda(m_q, \Delta_{\mathrm{gap}}; T = 0) = -\frac{N_f\Lambda^3}{\pi^2}\mu + \frac{N_f g_\Delta^2\Delta^2}{\pi^2}\mu\Lambda\left[1 - \frac{\sqrt{\mu^2 - m_q^2}}{\Lambda}\operatorname{artanh}\frac{\Lambda}{\sqrt{\mu^2 - m_q^2}} + \mathcal{O}(\Delta^2/\Lambda^2)\right]. \tag{E2}$$

Inserting this into the effective potential together with the bosonic potential Eq. (77) (with $Z_\Delta = 0$) and differentiating with respect to Δ to get the gap equation yields

$$\frac{\partial\Omega_{\mathrm{reg}}^{\mathrm{eff}}(\sigma, \Delta; T = 0)}{\partial\Delta} = \Delta\left\{2m_\Delta^2 + \frac{2N_f g_\Delta^2}{\pi^2}\mu\Lambda\left[1 - \frac{\sqrt{\mu^2 - m_q^2}}{\Lambda}\operatorname{artanh}\frac{\Lambda}{\sqrt{\mu^2 - m_q^2}} + \mathcal{O}(\Delta^2/\Lambda^2)\right]\right\} = 0. \tag{E3}$$

For the nontrivial finite solution $\Delta = \bar{\Delta}$, the expression in braces vanishes. The critical chemical potential μ_c, where $\bar{\Delta} \to 0$ (and $g_\phi\bar{\sigma} = \bar{m}_q$), is thus determined by the condition

$$2m_\Delta^2 + \frac{2N_f g_\Delta^2}{\pi^2}\mu_c\Lambda\left[1 - \frac{\sqrt{\mu_c^2 - \bar{m}_q^2}}{\Lambda}\operatorname{artanh}\frac{\Lambda}{\sqrt{\mu_c^2 - \bar{m}_q^2}}\right] = 0, \tag{E4}$$

which can be solved numerically to obtain μ_c once $\bar{m}_q$ is known (Note that μ_c should still satisfy the condition $\mu_c > \sqrt{\Lambda^2 + \bar{m}_q^2}$). Accordingly, a cutoff-dependent critical chemical potential μ_c emerges, and its very appearance signals a cutoff artifact of the regularized approximation. Furthermore, setting $\Delta = 0$ in Eq. (E2) leaves only the term linear in μ

$$L_\Lambda(m_q, \Delta_{\mathrm{gap}} = 0; T = 0) = -\frac{N_f\Lambda^3}{\pi^2}\mu. \tag{E5}$$

Because the bosonic potential in Eq. (77) is μ-independent without diquarks and the loop contribution Eq. (E5) is σ-independent, the gap equation reduces to the tree-level condition

$$-c + m_\phi^2\bar{\sigma} + \lambda_\phi\bar{\sigma}^3 = 0. \tag{E6}$$

Using the vacuum parameters listed in Table II, this yields a μ-independent constituent quark mass of $\bar{m}_q = 6.31$ MeV at large chemical potentials in the regMFA. This result is in perfect agreement with the values shown in Fig. 2. Inserting

this value into Eq. (E4), we get $\mu_c = 686.5$ MeV, in perfect agreement with the boundaries found in Figs. 1 and 2.

Furthermore, since $\bar{m}_q(\mu)$ is constant, the only μ-dependence in the pressure originates from the linear term in Eq. (E5). Consequently, the pressure scales as $p \propto \mu$ (in contrast to the μ^4 behavior in the Stefan-Boltzmann limit), and the corresponding energy density $\epsilon = -p + \mu \frac{dp}{d\mu}$ becomes μ-independent. As a result, the squared speed of sound, $c_s^2 = \frac{dp}{d\epsilon} = \frac{dp}{d\mu}(\mu \frac{d^2p}{d\mu^2})^{-1}$, diverges at large μ in the regularized model, as illustrated in Fig. 4.

APPENDIX F: NUMERICAL IMPLEMENTATION

Numerical results presented in this work are obtained using the `SciML` ecosystem offered by the `Julia` language. In particular, `Optimization.jl` [76] and solvers accessible within [77,78]. We also made use of automatic differentiation through `ForwardDiff.jl` [79] in the numerical computation of vacuum parameters, the entropy density, number densities and the speed of sound (by means of the Jacobian method developed in Ref. [80]). All figures are produced using `Makie.jl` [81].

[1] G. Aarts *et al.*, Phase transitions in particle physics: Results and perspectives from lattice quantum chromo-dynamics, Prog. Part. Nucl. Phys. **133**, 104070 (2023).
[2] C. S. Fischer, QCD at finite temperature and chemical potential from Dyson–Schwinger equations, Prog. Part. Nucl. Phys. **105**, 1 (2019).
[3] W.-j. Fu, QCD at finite temperature and density within the fRG approach: An overview, Commun. Theor. Phys. **74**, 097304 (2022).
[4] M. Buballa, NJL model analysis of dense quark matter, Phys. Rep. **407**, 205 (2005).
[5] B.-J. Schaefer and J. Wambach, The phase diagram of the quark meson model, Nucl. Phys. **A757**, 479 (2005).
[6] K. Fukushima and T. Hatsuda, The phase diagram of dense QCD, Rep. Prog. Phys. **74**, 014001 (2011).
[7] M. G. Alford, A. Schmitt, K. Rajagopal, and T. Schäfer, Color superconductivity in dense quark matter, Rev. Mod. Phys. **80**, 1455 (2008).
[8] J. Berges and K. Rajagopal, Color superconductivity and chiral symmetry restoration at nonzero baryon density and temperature, Nucl. Phys. **B538**, 215 (1999).
[9] T. M. Schwarz, S. P. Klevansky, and G. Papp, The phase diagram and bulk thermodynamical quantities in the NJL model at finite temperature and density, Phys. Rev. C **60**, 055205 (1999).
[10] J. Braun, M. Leonhardt, and J. M. Pawlowski, Renormalization group consistency and low-energy effective theories, SciPost Phys. **6**, 056 (2019).
[11] J. O. Andersen and M. P. Nødtvedt, Color superconductivity and speed of sound in the two-flavor quark-meson diquark model, Phys. Rev. D **111**, 034031 (2025).
[12] J. O. Andersen and M. P. Nødtvedt, Pion condensation versus 2SC, speed of sound, and charge neutrality effects in the quark-meson diquark model, Phys. Rev. D **113**, 014026 (2026).
[13] J. B. Kogut, M. A. Stephanov, and D. Toublan, On two color QCD with baryon chemical potential, Phys. Lett. B **464**, 183 (1999).
[14] J. O. Andersen and T. Brauner, Phase diagram of two-color quark matter at nonzero baryon and isospin density, Phys. Rev. D **81**, 096004 (2010).
[15] N. Strodthoff, B.-J. Schaefer, and L. von Smekal, Quark-meson-diquark model for two-color QCD, Phys. Rev. D **85**, 074007 (2012).
[16] R. L. S. Farias, G. Dallabona, G. Krein, and O. A. Battistel, Cutoff-independent regularization of four-fermion interactions for color superconductivity, Phys. Rev. C **73**, 018201 (2006).
[17] H. Gholami, M. Hofmann, and M. Buballa, Renormalization-group consistent treatment of color superconductivity in the NJL model, Phys. Rev. D **111**, 014006 (2025).
[18] C. Wetterich, Exact evolution equation for the effective potential, Phys. Lett. B **301**, 90 (1993).
[19] T. K. Herbst, M. Mitter, J. M. Pawlowski, B.-J. Schaefer, and R. Stiele, Thermodynamics of QCD at vanishing density, Phys. Lett. B **731**, 248 (2014).
[20] K. Iida, T. Matsuura, M. Tachibana, and T. Hatsuda, Melting pattern of diquark condensates in quark matter, Phys. Rev. Lett. **93**, 132001 (2004).
[21] P. Rehberg, S. P. Klevansky, and J. Hüfner, Hadronization in the SU(3) Nambu-Jona-Lasinio model, Phys. Rev. C **53**, 410 (1996).
[22] V. Skokov, B. Friman, E. Nakano, K. Redlich, and B. J. Schaefer, Vacuum fluctuations and the thermodynamics of chiral models, Phys. Rev. D **82**, 034029 (2010).
[23] S. R. Coleman and E. J. Weinberg, Radiative corrections as the origin of spontaneous symmetry breaking, Phys. Rev. D **7**, 1888 (1973).
[24] D. T. Son, Superconductivity by long range color magnetic interaction in high density quark matter, Phys. Rev. D **59**, 094019 (1999).
[25] T. Schäfer and F. Wilczek, Superconductivity from perturbative one gluon exchange in high density quark matter, Phys. Rev. D **60**, 114033 (1999).
[26] D. Nickel, R. Alkofer, and J. Wambach, On the unlocking of color and flavor in color-superconducting quark matter, Phys. Rev. D **74**, 114015 (2006).
[27] D. Nickel, J. Wambach, and R. Alkofer, Color-superconductivity in the strong-coupling regime of Landau gauge QCD, Phys. Rev. D **73**, 114028 (2006).
[28] D. Nickel, R. Alkofer, and J. Wambach, Neutrality of the color-flavor-locked phase in a Dyson-Schwinger approach, Phys. Rev. D **77**, 114010 (2008).

[29] F. Marhauser, D. Nickel, M. Buballa, and J. Wambach, Color-spin locking in a selfconsistent Dyson-Schwinger approach, Phys. Rev. D **75**, 054022 (2007).
[30] D. Müller, M. Buballa, and J. Wambach, Dyson-Schwinger approach to color superconductivity at finite temperature and density, Eur. Phys. J. A **49**, 96 (2013).
[31] D. Müller, M. Buballa, and J. Wambach, Dyson-Schwinger approach to color-superconductivity: Effects of self-consistent gluon dressing, arXiv:1603.02865.
[32] N. Khan, J. M. Pawlowski, F. Rennecke, and M. M. Scherer, The phase diagram of QC2D from functional methods, arXiv:1512.03673.
[33] J. Braun and B. Schallmo, From quarks and gluons to color superconductivity at supranuclear densities, Phys. Rev. D **105**, 036003 (2022).
[34] J. Cruz Rojas, T. Demircik, C. Ecker, and M. Järvinen, Towards holographic color superconductivity in QCD, arXiv:2505.06338.
[35] B. B. Brandt, V. Chelnokov, G. Endrődi, G. Marko, D. Scheid, and L. von Smekal, Renormalization group invariant mean-field model for QCD at finite isospin density, Phys. Rev. D **112**, 054038 (2025).
[36] S. Carignano, M. Buballa, and B.-J. Schaefer, Inhomogeneous phases in the quark-meson model with vacuum fluctuations, Phys. Rev. D **90**, 014033 (2014).
[37] S. Carignano, M. Buballa, and W. Elkamhawy, Consistent parameter fixing in the quark-meson model with vacuum fluctuations, Phys. Rev. D **94**, 034023 (2016).
[38] J. M. Pawlowski, Aspects of the functional renormalisation group, Ann. Phys. (Amsterdam) **322**, 2831 (2007).
[39] J. M. Pawlowski, M. M. Scherer, R. Schmidt, and S. J. Wetzel, Physics and the choice of regulators in functional renormalisation group flows, Ann. Phys. (Amsterdam) **384**, 165 (2017).
[40] D. Bailin and A. Love, Superfluidity and superconductivity in relativistic fermion systems, Phys. Rep. **107**, 325 (1984).
[41] J. A. Bowers and K. Rajagopal, The crystallography of color superconductivity, Phys. Rev. D **66**, 065002 (2002).
[42] D. K. Hong, An effective field theory of QCD at high density, Phys. Lett. B **473**, 118 (2000).
[43] K. Rajagopal and F. Wilczek, The condensed matter physics of QCD, in *At the Frontier of Particle Physics. Handbook of QCD. Vol. 1-3*, edited by M. Shifman and B. Ioffe (World Scientific, 2000), pp. 2061–2151.
[44] M. Huang and I. A. Shovkovy, Screening masses in neutral two-flavor color superconductor, Phys. Rev. D **70**, 094030 (2004).
[45] R. D. Pisarski and D. H. Rischke, Color superconductivity in weak coupling, Phys. Rev. D **61**, 074017 (2000).
[46] J. Braun, T. Dörnfeld, B. Schallmo, and S. Töpfel, Renormalization group studies of dense relativistic systems, Phys. Rev. D **104**, 096002 (2021).
[47] J. Braun and B. Schallmo, Zero-temperature thermodynamics of dense asymmetric strong-interaction matter, Phys. Rev. D **106**, 076010 (2022).
[48] J. Deng, A. Schmitt, and Q. Wang, Relativistic BCS-BEC crossover in a boson-fermion model, Phys. Rev. D **76**, 034013 (2007).
[49] I. A. Shovkovy and P. J. Ellis, Thermal conductivity of dense quark matter and cooling of stars, Phys. Rev. C **66**, 015802 (2002).
[50] K. Rajagopal and F. Wilczek, Enforced electrical neutrality of the color flavor locked phase, Phys. Rev. Lett. **86**, 3492 (2001).
[51] K. Fukushima and S. Minato, Speed of sound and trace anomaly in a unified treatment of the two-color diquark superfluid, the pion-condensed high-isospin matter, and the 2SC quark matter, Phys. Rev. D **111**, 094006 (2025).
[52] B. A. Freedman and L. D. McLerran, Fermions and gauge vector mesons at finite temperature and density. 3. The ground state energy of a relativistic quark gas, Phys. Rev. D **16**, 1169 (1977).
[53] A. Kurkela, P. Romatschke, and A. Vuorinen, Cold quark matter, Phys. Rev. D **81**, 105021 (2010).
[54] A. Kurkela and A. Vuorinen, Cool quark matter, Phys. Rev. Lett. **117**, 042501 (2016).
[55] T. Gorda, A. Kurkela, P. Romatschke, S. Säppi, and A. Vuorinen, Next-to-next-to-next-to-leading order pressure of cold quark matter: Leading logarithm, Phys. Rev. Lett. **121**, 202701 (2018).
[56] Y. Fujimoto and K. Fukushima, Equation of state of cold and dense QCD matter in resummed perturbation theory, Phys. Rev. D **105**, 014025 (2022).
[57] A. Geißel, T. Gorda, and J. Braun, Pressure and speed of sound in two-flavor color-superconducting quark matter at next-to-leading order, Phys. Rev. D **110**, 014034 (2024).
[58] A. Geißel, T. Gorda, and J. Braun, Color superconductivity under neutron-star conditions at next-to-leading order, Phys. Rev. Lett. **135**, 211901 (2025).
[59] M. Hess, F. Karsch, E. Laermann, and I. Wetzorke, Diquark masses from lattice QCD, Phys. Rev. D **58**, 111502(R) (1998).
[60] M. Oettel, R. Alkofer, and L. von Smekal, Nucleon properties in the covariant quark diquark model, Eur. Phys. J. A **8**, 553 (2000).
[61] P. Maris, Effective masses of diquarks, Few Body Syst. **32**, 41 (2002).
[62] K. Otto, M. Oertel, and B.-J. Schaefer, Hybrid and quark star matter based on a nonperturbative equation of state, Phys. Rev. D **101**, 103021 (2020).
[63] M. Leonhardt, M. Pospiech, B. Schallmo, J. Braun, C. Drischler, K. Hebeler, and A. Schwenk, Symmetric nuclear matter from the strong interaction, Phys. Rev. Lett. **125**, 142502 (2020).
[64] H. Gholami, I. A. Rather, M. Hofmann, M. Buballa, and J. Schaffner-Bielich, Astrophysical constraints on color-superconducting phases in compact stars within the RG-consistent NJL model, Phys. Rev. D **111**, 103034 (2025).
[65] A. E. B. Pasqualotto, R. L. S. Farias, W. R. Tavares, S. S. Avancini, and G. Krein, Causality violation and the speed of sound of hot and dense quark matter in the Nambu–Jona-Lasinio model, Phys. Rev. D **107**, 096017 (2023).
[66] G. Baym, T. Hatsuda, T. Kojo, P. D. Powell, Y. Song, and T. Takatsuka, From hadrons to quarks in neutron stars: A review, Rep. Prog. Phys. **81**, 056902 (2018).
[67] L. Bonanno and A. Sedrakian, Composition and stability of hybrid stars with hyperons and quark color-superconductivity, Astron. Astrophys. **539**, A16 (2012).

[68] T. Klähn, R. Łastowiecki, and D. B. Blaschke, Implications of the measurement of pulsars with two solar masses for quark matter in compact stars and heavy-ion collisions: A Nambu–Jona-Lasinio model case study, Phys. Rev. D **88**, 085001 (2013).
[69] K. Otto, M. Oertel, and B.-J. Schaefer, Nonperturbative quark matter equations of state with vector interactions, Eur. Phys. J. Spec. Top. **229**, 3629 (2020).
[70] M. Buballa, L. Kurth, M. Wagner, and M. Winstel, Regulator dependence of inhomogeneous phases in the $(2+1)$-dimensional Gross-Neveu model, Phys. Rev. D **103**, 034503 (2021).
[71] L. Pannullo, M. Wagner, and M. Winstel, Inhomogeneous phases in the $3+1$-dimensional Nambu-Jona-Lasinio model and their dependence on the regularization scheme, Proc. Sci., LATTICE2022 (**2023**) 156 [arXiv:2212.05783].
[72] L. Pannullo, M. Wagner, and M. Winstel, Regularization effects in the Nambu–Jona-Lasinio model: Strong scheme dependence of inhomogeneous phases and persistence of the moat regime, Phys. Rev. D **110**, 076006 (2024).
[73] H. Gholami, L. Kurth, U. Mire, M. Buballa, and B.-J. Schaefer, Ancillary files for: Renormalizing the Quark-Meson-Diquark model, https://arxiv.org/src/2505.22542/anc (2025).
[74] R. M. Corless, G. H. Gonnet, D. E. G. Hare, D. J. Jeffrey, and D. E. Knuth, On the Lambert W function, Adv. Comput. Math. **5**, 329 (1996).
[75] NIST Digital Library of Mathematical Functions, Lambert W-function (2024), release 1.2.3, accessed 22 May 2025.
[76] V. K. Dixit and C. Rackauckas, Optimization.jl: A unified optimization package (2023).
[77] S. G. Johnson, The NLopt nonlinear-optimization package, https://github.com/stevengj/nlopt (2007).
[78] J. A. Nelder and R. Mead, A simplex method for function minimization, Comput. J. **7**, 308 (1965).
[79] J. Revels, M. Lubin, and T. Papamarkou, Forward-mode automatic differentiation in Julia, arXiv:1607.07892.
[80] H. Gholami, On the calculation of pressure derivatives in mean-field thermal field theories, arXiv:2501.05192.
[81] S. Danisch and J. Krumbiegel, Makie.jl: Flexible high-performance data visualization for Julia, J. Open Source Software **6**, 3349 (2021).